MASTER'S THESIS

Testing the accuracy of Aerosol Optical Depth retrievals from the EKO MS-711

ETH ZÜRICH

Institute for Atmospheric and Climate Science
Department Environmental Systems Science

Submitted by

Davide Rezzonico
redavide@student.ethz.ch
17-931-981

Supervisors

John A. Augustine
Laura D. Riihimaki
Martin Wild

Zürich, April 2024

Measurement is the first step that leads to control and eventually to improvement. If you can't measure something, you can't understand it. If you can't understand it, you can't control it. If you can't control it, you can't improve it.

- H. James Harrington (2021)

Acknowledgments

A special thanks go to John A. Augustine and Dr. Laura D. Riihimaki for their tremendous availability and advice dispensed for the understanding, processing and analyzing of the data. Without their precious contributions, this work would not have been possible. I also thank Charles Wilson for his incredible work in the laboratory, Dr. Connor Flynn for his valuable suggestions and Prof. Dr. Martin Wild for his remote help.

A final acknowledgment goes to everyone who actively and passively supported me, including everyone of GRAD group at NOAA, my family, friends, and my girlfriend Sofia.

Abstract

According to the IPCC, aerosols in the atmosphere play an uncertain role in affecting the Earth's climate system (IPCC 2022). A deep understanding of these constituents is therefore necessary in order to implement climate policies and strategies. Measuring the direct component (i.e. a part of the solar irradiance that directly reaches a surface) spectrally makes it possible to infer for various wavelengths the aerosol optical depth (AOD). This number is a measure of extinction (or attenuation) by aerosols in the vertical column, and it is directly related to the concentration of aerosols in the air. Currently, sun photometers such as the Precision Filter Radiometers (PFR), Cimel, and SP02 are among the most common instruments for monitoring AOD. The Multifilter Rotating Shadowband Radiometer (MFRSR) is another class of sun photometer that uses a shade band to allow global and diffuse spectral measurements from which the direct component can be derived for AOD. The EKO MS-711 is another shadow band instrument that provides continuous spectral information and a better coverage compared to the more common sun photometers with limited discrete spectral channels.

This research investigated the potential of the EKO MS-711 spectroradiometer, in order to understand whether the accuracy of this instrument is sufficient to encourage widespread adoption for aerosol optical depth monitoring.
For each spectral channel considered, Langley calibrations (namely the expected direct-normal signal at the top of the atmosphere) were produced for clear-sky days within a two-month period using the AOD-retrieval method, which is based on the Beer-Lambert law. Time series of those spectral calibrations were fit to linear functions that were used to interpolate calibration values to any day in the analysis period. In this way, AOD retrievals from the EKO MS-711 were compared to those of the MFRSR, at MFRSR wavelengths for which interference by constituents other than aerosols is minimal. In the laboratory, the behavior of this device was investigated as the angle of incidence of radiation varies (cosine response) and cosine corrected AOD retrievals from both instruments were compared. Furthermore, the Ängstrom exponent, a unitless number that characterizes the wavelength dependence of AOD and provides information on the relative size of the aerosols present in the column, was evaluated.

The results revealed that it is essential to apply a cosine correction to obtain accurate AOD values. In particular, the cosine response measured at the NOAA Central UV Calibration Facility (CUCF) Laboratory was shown to be more accurate than the one provided by the manufacturer. The comparison between EKO MS-711-derived AOD and MFRSR-retrieved AOD at MFRSR wavelengths revealed a satisfactory degree of agreement, although some systematic deviations were detected. In particular, it was demonstrated that the 868 nm channel has the greatest noise, whereas the 415 nm channel has the greatest mismatch, being the only channel consistently falling outside the acceptability limits set by PMOD/WRC with respect to the MFRSR. Various uncertainties and inaccuracies were documented, such as the malfunction of the MFRSR at 415 nm, a tilting of the MFRSR toward the South-East direction, and inaccuracies in the rotating shadow band and in the software of the EKO MS-711. In addition, concerns arose related to the two-month period of data analyzed; it was too short on the one hand and affected by extremely low AOD values on the other.

At the present state, the EKO MS-711 exhibits too many unknowns to be able to replace existing distinct-channel sun photometers such as the MFRSR. However, future transition to the EKO-711 seems to be possible as long as significant research and improvements are made, and that extensive long-term intercomparison campaigns are conducted to validate the quality of the EKO MS-711. This would open new doors for research, with the possibility of investigating the behavior of various atmospheric constituents (such as for instance water vapor and sulphur dioxide) with greater confidence.

Contents

List of Figures

List of Tables

List of Symbols

Irradiance measurement

DHI	Diffuse Horizontal Irradiance
DNI	Direct Normal Irradiance
GHI	Global Horizontal Irradiance, Shadowband position 1
GHI^{+}	Global Horizontal Irradiance, Shadowband position 2
GHI^{-}	Global Horizontal Irradiance, Shadowband position 4
I_{λ}	Direct normal irradiance at the surface for wavelength λ
$I_{\lambda 0}$	Direct normal irradiance at TOA for wavelength λ
V	Voltage measurement at the surface for wavelength λ
V_0	Voltage measurement at TOA for wavelength λ

Quantities related to aerosol measurement

AOD	Aerosol Optical Depth
α	Ängstrom exponent
τ	Optical Depth

Quantities related to solar angle

ϕ	Solar Azimuth Angle
Θ	Solar Zenith Angle
m	Path length

Acronyms

TOA	Top of Atmosphere
RSB	Rotating Shadowband

1 Introduction

Of the many different forcing factors affecting climate change, it has been shown that the effect of aerosols can partly counteract the warming due to the increasing carbon dioxide (e.g. Augustine, Cornwall, et al. 2003). However, different aerosols affect the temperature in different ways. Black carbon particles (soot) absorb solar radiation and heat the atmosphere, whereas scattering aerosols, such as sulphate particles emitted by volcanic eruptions, have a cooling effect on the system (Wild 2022). In addition, aerosols may affect the properties of clouds by acting as cloud condensation nuclei and they modify climate indirectly through cloud radiative effects (e.g. IPCC 2022, Myhre et al. 2013, Arola et al. 2022). A precise measurement and monitoring of all the aerosol forcings is therefore necessary in order to understand our climate and eventually implement appropriate climate change mitigation policies (Hansen et al. 2000).

1.1 State of the art

In the United States, there are various aerosol optical depth (AOD) monitoring networks employing different automated instruments. One such network is the National Aeronautics and Space Administration (NASA) Aerosol Robotic Network (AERONET), established in 1993, which relies on sun photometers, such as for instance Precision Filter Radiometers (PFR), Cimel's, and SP02. Other U.S. networks, including the National Oceanic and Atmospheric Administration's (NOAA) Surface Radiation Budget Network (SURFRAD, Augustine, DeLuisi, and Long 2000; Augustine, Hodges, Cornwall, et al. 2005), the Department of Energy (DOE) Atmospheric Radiation Measurement Program (ARM, Augustine, Cornwall, et al. 2003), and the Quantitative Links program (QL, J. J. Michalsky, Schlemmer, et al. 2001), use the Multifilter Rotating Shadowband Radiometer (MFRSR).
These instruments measure the solar spectral component, allowing for the inference of aerosol optical depth through the AOD-retrieval method, as introduced in Section 1.2 and expanded in Section 4.2.

1.2 Beer-Lambert-Bouguer law

Attenuation by aerosols in the atmosphere can be determined by computing the aerosol optical depth, a dimensionless number that describes spectral radiation extinction by aerosols in the vertical column over the observation location, and is a qualitative indication of the number of aerosols in the column. The AOD is derived from sunlight attenuation measurements in the atmospheric path (García-Cabrera et al. 2020). The attenuation of a solar beam in the atmosphere can be described by the Beer-Lambert–Bouguer law (Equation 1, Augustine, Cornwall, et al. 2003):

$$I_\lambda = I_{\lambda 0} \cdot exp[-m \cdot \sum \tau(\lambda)] \tag{1}$$

where I_λ is the direct normal irradiance at the surface for wavelength λ measured by the instrument, $\mathrm{I}_{\lambda 0}$ is the direct normal irradiance for λ at the top of atmosphere, $\mathrm{m} = 1/\cos(\Theta)$[1] is the optical mass (path through a curved atmosphere, where Θ is defined as the solar zenith angle) and $\sum\tau(\lambda)$ is the total optical depth of atmosphere for radiation at wavelength λ.

In the UV-VIS range (100-800 nm), the total optical depth $\sum\tau(\lambda)$ is primarily made of contributions from aerosol ($\tau_\mathrm{a}(\lambda)$), Rayleigh molecular scattering ($\tau_\mathrm{R}(\lambda)$), and absorption of atmospheric gases in the affected wavelengths, such as ozone, dioxygen, nitrogen dioxide and water vapor ($\tau_{\mathrm{O_3}}(\lambda)$, $\tau_{\mathrm{O_2}}(\lambda)$, $\tau_{\mathrm{NO_2}}(\lambda)$ and $\tau_{\mathrm{H_2O}}(\lambda)$, respectively) (García et al. 2021) according to Equation 2:

$$\sum \tau(\lambda) = \tau_\mathrm{a}(\lambda) + \tau_\mathrm{R}(\lambda) + \tau_{\mathrm{O_3}}(\lambda) + \tau_{\mathrm{O_2}}(\lambda) + \tau_{\mathrm{NO_2}}(\lambda) + \tau_{\mathrm{H_2O}}(\lambda) \tag{2}$$

To get aerosol optical depth, the contributions from molecular scattering and absorption by these various gases must be subtracted from the measured total optical depth.

[1]Equation 12 provides a better estimate for the path length, also accounting for curvature effects.

Figure 1 shows a schematic of the shortwave radiative transfer through the atmosphere.

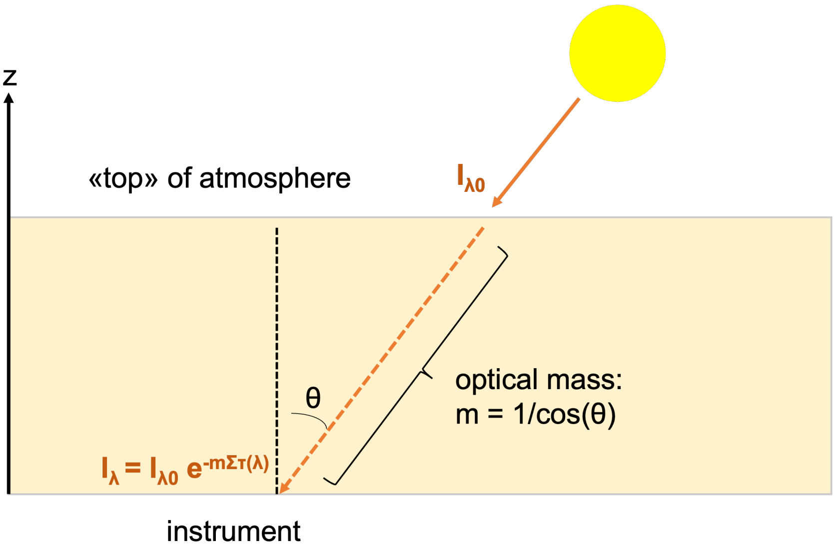

Figure 1: Schematic of the shortwave radiative transfer through a curved atmosphere as described by the Lambert–Bouguer law. Adapted from Wild 2022.

The optical depth for a particular atmospheric component is described by Equation 3:

$$\tau(\lambda) = \int_{z=0}^{z} k_\lambda \cdot \rho(z)\, dz \tag{3}$$

where $\rho(z)$ is the density of the constituent at height z above the surface and k_λ is the extinction coefficient which is very dependent on the wavelength (different gases absorb at different wavelengths). It should be noted that the extinction coefficient k_λ is the sum of the absorption and scattering coefficient, $k_{\lambda,abs}$ and $k_{\lambda,scatt}$, respectively.

2 Objectives

Traditionally, many of the aerosol optical depth measurements around the world have been made with filter-based instruments (cfr. Section 1.1), because it is easier to get an accurate spectral measurement as there is generally a higher signal-to-noise ratio from the chosen wavelengths. However, the limitation to a certain set of wavelengths allows a radiometer device to detect and measure electromagnetic radiation only within a narrow range.
Given its capacity to provide measurements with a full spectrum range (300 - 1100 nm, cfr. Section 3), as opposed to discrete narrowband filters as in the MFRSRs as well as sun photometers, a spectrometer instrument like the EKO MS-711 could have the potential to give more, somewhat continuous, information[2].

The primary purpose of this work is therefore to assess how well the EKO MS-711-derived AOD compares to MFRSR-retrieved AOD at MFRSR wavelengths. More specifically, the objective is to determine whether the accuracy of the EKO MS-711 is sufficient to replace existing distinct-channel sun photometers such as the MFRSR.

The EKO MS-711 was first installed at Table Mountain, followed by laboratory testing to assess its cosine response. These two steps aim to gain a comprehensive understanding of the instrument's installation, operational procedures, accuracy, and, if required, maintenance. A final section will be dedicated to the discussion of the possible corrections that could improve the retrieval.

[2] Better coverage as they can detect and measure a wider spectrum of wavelengths.

3 Instrumentation

The data used in this work have been gathered by the EKO MS-711 installed at the SURFRAD station located on Table Mountain in Boulder, Colorado (cfr. Figure A1 Appendix A.1). After having collected the data, the instrument was taken to the laboratory to measure the cosine response. Both the measured and the manufacturer-supplied cosine correction have been applied to see which one produces AODs closest to those from the MFRSR measurements.

3.1 EKO MS-711

The EKO MS-711 is an all-weather sensor with a temperature-controlled detector core that provides irradiance measurements within the 300 - 1100 nm (UV-Visible-NIR) spectral range at a resolution of about 0.4 nm (CO 2016). This spectroradiometer instrument collects incoming global solar radiation in a 180° field of view, followed by diffuse solar measurement with the help of a shading band.
Inside the instrument, incoming light is first dispersed into its individual wavelengths by a spectroscope (or grating). Subsequently, a Charge-Coupled Device (CCD) - a linear series of 2048 silicon detectors - is used to detect the intensity of photons at consecutive wavelengths at a resolution of about 0.4 nm. When light hits the surface of the CCD, it induces the release of electrons in the semiconductor material. The quantity of released electrons - directly proportional to the intensity of the incident light - translates into a measured signal. For further details regarding the key components of the spectrometer, please refer to Figure A2 in Appendix A.2.
The version of the EKO MS-711 available at Table Mountain is mounted in a box and equipped with a rotating shadow band (RSB), so it operates the same as an MFRSR. In this configuration, a narrow band changes its position intermittently to cast and remove shade over the detector. This allows for sequential measurements of global and diffuse irradiance, enabling the calculation of direct normal irradiance (DNI). More precisely, as the RSB rotates, four measurements are captured in less than 1 minute for four different shadow band positions (Pó et al. 2018). This principle is shown schematically in Figure 2 and in photographs in Figure 3.

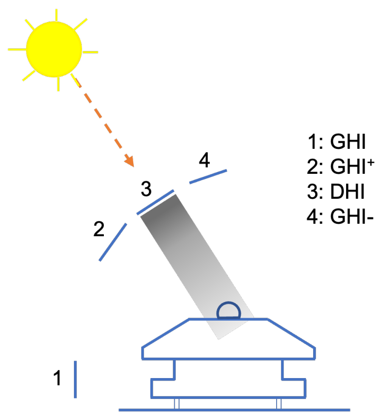

Figure 2: Rotating shadow band sweeping positions. Adapted from Pó et al. 2018.

To measure the global horizontal irradiance, the RSB rests outside of the instrument field of view, to avoid any interference (position 1, *rest*). For the measurement of the diffuse component, it is necessary to remove the direct from the global component. This is the case when the RSB is located exactly between the instrument and the sun, covering the solar disk and shading the dome completely (position 3). In this process, a portion of the DHI is lost due to RSB sky coverage. To account for this, measuring the global irradiance obstructed by the presence of the shadow band at positions 2 and 4, namely at ± 10° from the sun disk, allows for corrections to be applied to the DHI, as detailed in Section 4.1.2.

Figure 3 shows the positioning of the RSB under real operating conditions.

Figure 3: From left to right: GHI, GHI^{+}, DHI, GHI^{-} measurement (RSB position 1-4).

EKO MS-711 measures with a bin width of 0.4 nm and a bandpass of nominally < 7 nm, defined as the full width at half maximum (FWHM). The measures of the irradiance components are performed with a temporal resolution of 1 minute, with the integration time of each measurement varying between 10 ms to 5 s, depending on the light intensity (García et al. 2021).
Table 1 reports all the main specifications of the EKO MS-711 spectroradiometer.

Table 1: Main specifications of the EKO MS-711 spectroradiometer (Pó et al. 2018).

	Specifications
Wavelength range	300 - 1100 nm
Optical resolution FWHM	$<$ 7 nm
Wavelength accuracy	$\pm$ 0.2 nm
Directional response (cosine response (0-80°))	$<$ 5%
Temperature response -10° to 50°C	$<$ 2%
Temperature control	25 $\pm$ 2°C
Operating temperature range	-10° to 50°C
Exposure time	10 to 5000 msec
Field of view	180°
Dome material	Synthetic quartz glass
Communication	RS-422 (between sensor and power supply)
Power requirment	12 VDC, 50 VA

3.2 Multifilter Rotating Shadow band Radiometer (MFRSR)

Global and diffuse components of solar irradiance at up to seven wavelengths can be measured by the Multifilter Rotating Shadowband Radiometer (MFRSR, NOAA 2022). Unlike the EKO MS-711, which measures continuously, the MFRSR is equipped with a set of narrowband optical filters, each allowing only a specific range of wavelengths to pass through. These filters are strategically selected to capture solar radiation at various discrete wavelengths. The instrument is provided with an array of seven filtered silicon detectors that are associated with each of the wavelengths of interest. These detectors measure the solar irradiance passing through the filters as the number of electrons released thus providing a corresponding signal.
In the same way as the EKO MS-711, a shadow band alternately shades and exposes the instrument diffuser, permitting the device to measure diffuse and global irradiance with only one detector. Table 2 provides the main characteristic for MFRSR instruments.

Table 2: Main specifications of the MFRSR (NOAA 2022).

	Specifications
Spectral range	1 broadband channel 6 additional narrowband channels centered on: 415, 499, 673, 870, and 940, 1625 nm[1]
Optical resolution FWHM	10 nm
Cosine response	Better than 5% for 0 - 80° Θ; better than 1% with corrections
Temperature range	-30° to 50°C
Temporal resolution	15-20 s

[1] The 1625 nm channel relies on the InGaAs detector (Indium, Gallium, Arsinide detector).

Depending on the atmospheric components one wants to investigate, one narrowband is preferable to another. For instance, the 940 nm channel can be used to gain information about the column water vapor, whereas the 415 nm and 499 nm bands can be used to infer column ozone (J. J. Michalsky, Liljegren, and L. C. Harrison 1995; J. J. Michalsky and Kiedron 2022).
With diffuse measurements available, aerosol parameters such as single scattering albedo and size distribution can also be estimated. The 1625 nm channel was added to expand the size distribution range in order to include coarse mode aerosols.

4 Methods

4.1 Data extraction and processing

4.1.1 Measured values

The EKO MS-711 instrument provides minute data in the wavelength range between 300-1100 nm with a resolution of 0.4 nm. The main measured data are shown in Table 3 following the principle illustrated schematically in Section 3.1 (cfr. Figure 2)

Table 3: Main data measured by the EKO MS-711 instrument.

Data measured	Features & symbols
Time	Hour, minute, second
Wavelength	2048 pixels, every 0.4 nm
Global horizontal irradiance, RSB position 1	GHI
Global horizontal irradiance, RSB position 2	GHI^+
Diffuse horizontal irradiance, RSB position 3	DHI
Global horizontal irradiance, RSB position 4	GHI^-
Azimuth angle	ϕ
Solar zenith angle	Θ

Other data provided include exposure time, elevation angle, solar shade angle and edge angle. Latitude and longitude are also supplied, at Table Mt. 40.125 °N and 105.237 °W, respectively.

Given that the overarching objective of the project is to conduct a comparison between the EKO MS-711 and the MFRSR instrument, it is logical to focus on the channels that are common to both instruments. Considering that the 940 nm channel is primarily utilized for water vapor retrieval (cfr. Figure B1 and Figure B2 Appendix B.1) and the EKO MS-711 instrument lacks measurements beyond 1100 nm, the relevant channels available for comparison are limited to the following four:

- Channel 1: 415 nm
- Channel 2: 499 nm
- Channel 3: 674 nm
- Channel 4: 868 nm

Examining the solar spectrum and the absorption bands across various wavelengths (cfr. Figure B1 and Figure B2 Appendix B.1), it is possible to identify the main components - besides aerosols - affecting the various wavelengths. It is expected that the Rayleigh scattering contribution decreases as the wavelength increases - resulting in a maximum value at 415 nm and a minimum at 868 nm - , whereas the ozone absorption contribution is biggest at 674 nm.
Table 4 briefly lists the different spectral contributions for the 4 channels (García-Cabrera et al. 2019).

Table 4: Wavelength and spectral corrections used for the AOD retrieval.

Wavelength [nm]	Spectral corrections
415	Rayleigh, O_3 (negligible)
499	Rayleigh, O_3, NO_2 (negligible)
674	Rayleigh, O_3
868	Rayleigh

4.1.2 Shading correction

As described in Section 3.1, a shading correction should be applied to the measured DHI. The lost portion of the diffuse component during the RSB covering the solar disk can be determined by calculating the difference between the global irradiance at position 1 and the average value of the global irradiance at positions 2 and 4, namely before and after full coverage. By adding this computed correction to the diffuse measurement, the actual diffuse horizontal irradiance for each wavelength at every given time can be derived. This relationship is expressed by Equation 4.

$$DHI_{\lambda,\text{ corr}} = DHI_{\lambda,\text{ measured}} + (GHI_\lambda - \frac{GHI^{+}{}_\lambda + GHI^{-}{}_\lambda}{2}) \tag{4}$$

4.1.3 FWHM correction

Since the FWHM bandpass of the EKO MS-711 slit function is 7 nm, selecting a certain wavelength also requires consideration of neighboring ones.

As depicted in Figure 4, using a Gaussian distribution (García-Cabrera et al. 2019), it is possible to assign weights to each measured value based on the distance from the central wavelength (channels 1-4). This slit function only depends on 2 parameters, namely the median (i.e. 415, 499, 674 and 868 nm, respectively) and the standard deviation σ. The relationship between FWHM and σ is given by Equation 5.

$$FWHM = \sqrt{8 \cdot ln(2)} \cdot \sigma \tag{5}$$

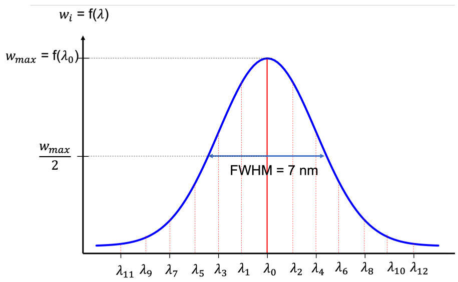

Figure 4: Gauss distribution used to assign the weights for each wavelength.

For all the wavelength values that lie within a distance ± 4σ from the median, a unique weight can be assigned. This weight should then be applied to all the measured irradiance values (DHI_{corr}, GHI^{+}, GHI^{-}, GHI) corresponding to these wavelengths. Equation 6 illustrates the correction that needs to be applied before computing the direct normal irradiance.

$$\text{value measured, FWHM} = \frac{\sum_{i=1}^{n}(w_{\text{i}} \cdot \text{value measured, i})}{\sum_{i=1}^{n} w_{\text{i}}} \tag{6}$$

4.1.4 DNI computation

After global and diffuse components have been accordingly corrected, it is possible to compute the direct normal irradiance. This can be achieved by leveraging the relationship among the 3 irradiance components with respect to a horizontal surface, as given by Equation 7.

$$Direct\ horizontal\ irradiance = GHI - DHI \tag{7}$$

To convert a direct value referenced to the horizontal plane to one normal to the sun, one only needs to consider the geometric relationship described in Equation 8.

$$DNI = \frac{Direct\ horizontal\ irradiance}{cos(\Theta)} \tag{8}$$

Combining Equations 4, 6, 7, and 8 enables the computation of the direct normal irradiance (DNI) for each wavelength and time step, as expressed in Equation 9.

$$DNI_\lambda = \frac{GHI_\lambda - DHI_{\lambda,\text{ corr}}}{cos(\Theta)} \tag{9}$$

It is noteworthy to mention that before making any computation, one should account for the dark offset of the instrument (which is the output of CCD elements when there is no incident radiation) and the dark counts should be subtracted from the solar measurements (Vignola, Michalsky, and Stoffel 2019). This step has already been carried out by the manufacturer and the signal has been removed from the data measured by the instrument.
Since the EKO MS-711 shuts down when Θ reaches 90° (i.e. before sunrise and after sunset), to verify that a dark signal exists, one needs only to place a cap over the dome of the sensor (hence simulating nighttime conditions) and record the measurements. Alternately, a similar procedure could be performed in the laboratory. In any case, considering that the possible presence of a dark offset signal affects every measured radiation component, this signal should be systematically subtracted from every measured irradiance. Equation 7 suggests that for DNI purposes this step can be omitted, because direct radiation is the difference of two measurements. Thus, even if a dark signal were present, it would cancel out, thus leaving the value of direct radiation independent of this offset. For other applications, however, a dark signal could very much affect the analysis.

4.1.5 Cosine correction

A common assumption made when employing devices that measure irradiance on a horizontal surface is that the response of the instrument decreases exactly as the cosine of the solar zenith angle, i.e. the cosine response is ideal (J.J. Michalsky, L. Harrison, and Berkheiser 1995). However, it is generally recognized that global irradiance devices do not have perfect cosine responses.
An ideal cosine response, which describes how irradiance on a horizontal surface varies naturally with the cosine of the zenith angle, is depicted in Figure 5. As the sun gets lower, the same amount of energy - represented by the top of the boxes, all normal to the sun - is spread out over a larger area on a horizontal surface, making the part of the beam that actually impacts the horizontal detector (such as the EKO MS-711 or the MFRSR) become smaller and thus less intense.

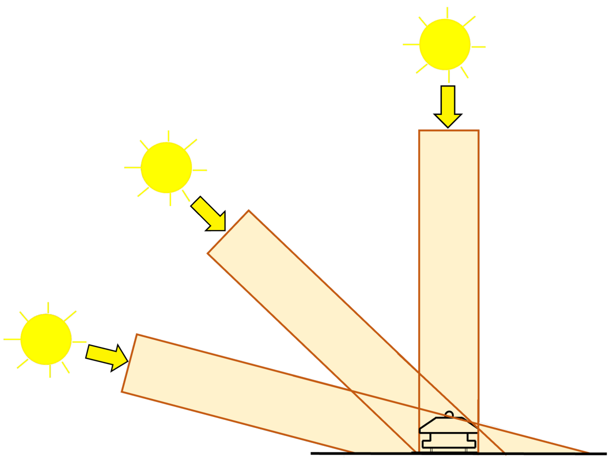

Figure 5: Ideal cosine response. This geometry defines 3 different angles of incident radiation with respect to the normal for a typical 2π sr field of view sensor (black instrument). Adapted from J.J. Michalsky, L. Harrison, and Berkheiser 1995.

The cosine correction is the difference between the ideal cosine response and what is actually measured. That difference should be added back to the measurement to remove the *cosine error*, caused by physical characteristics of the instrument. When the cosine correction is applied to the raw measurements, the resultant global horizontal values as a function of the solar zenith angle should resemble an ideal cosine response. Thus, the direct component can be computed with more confidence.
Before AOD processing, the DNI data computed from EKO MS-711 will be subjected to this procedure, using both the manufacturer's and the laboratory-measured cosine response.

Manufacturer

By mounting the instrument on an optical bench and using a solar simulator (AAA grade), the manufacturer (EKO Instruments Co., Ltd.) has performed a cosine response every 10° Θ in the four cardinal azimuth directions. The results reported in Table 5 represent the discrepancy relative to the ideal cosine response, computed by making use of Equation 10 (Pó et al. 2018; Vignola, Michalsky, and Stoffel 2019).

$$\text{Cosine correction} = (\frac{V_{\text{measured}}}{cos(\Theta)} - 1) \cdot 100\% \qquad (10)$$

where $V_{\text{measured}} = \frac{V_{\Theta}}{V_{\Theta=0}}$ represents the measured signal at incidence angle Θ normalized with respect to the measured signal at 0°. The ratio between V_{measured} and the ideal cosine of SZA provides a cosine correction for every solar zenith angle and azimuth direction considered.

Table 5: Cosine response of EKO MS-711 as provided by the manufacturer.

Θ [°]	South side error [%]	North side error [%]	East side error [%]	West side error [%]
0	0.00	0.00	0.00	0.00
10	0.47	0.88	0.79	1.04
20	1.10	1.84	1.32	1.07
30	1.24	2.13	1.62	1.45
40	1.19	2.66	2.27	1.68
50	1.34	3.11	2.45	1.98
60	1.59	4.25	3.09	2.21
70	0.75	4.46	2.52	1.93
80	-2.37	1.17	-1.40	-1.66

Figure 6 reports the data listed in Table 5 for the 4 azimuth directions.

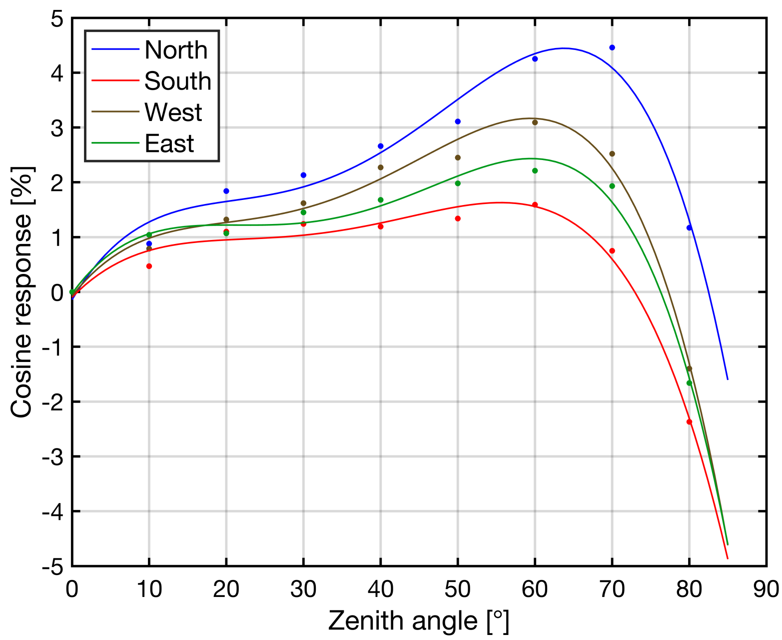

Figure 6: Cosine response of the EKO MS-711 for the 4 azimuth orientations as provided by the manufacturer. For each data set, a curve is fitted to the data.

For each orientation a third-order polynomial has been fit. The equations for the error ϵ as a function of the solar zenith angle Θ are listed in Table 6.

Table 6: Fitted cosine correction equations for south, north, east and west side. ϵ represents the error, Θ the solar zenith angle.

	Fitted equation
North side error	$\epsilon = 0.0003\Theta^3 - 0.0121\Theta^2 + 0.2370\Theta - 0.1407$
South side error	$\epsilon = 0.0002\Theta^3 - 0.0075\Theta^2 + 0.1442\Theta - 0.0971$
West side error	$\epsilon = 0.0002\Theta^3 - 0.0106\Theta^2 + 0.1930\Theta - 0.0277$
East side error	$\epsilon = 0.0002\Theta^3 - 0.0095\Theta^2 + 0.1790\Theta - 0.0741$

Based on the solar azimuth angle ϕ - an angular measurement that defines the direction from which the sunlight is coming at a specific location on the Earth's surface (and which provides information about the orientation of the sun in the horizontal plane with respect to an observer) -, it becomes feasible to assign weights to the error. This is shown in Figure 7. For instance, when $\phi = 10°$, it is necessary to apportion north and east corrections based on the position of the solar azimuth. In this particular scenario, 1/9 of the total error is attributed to the east component, while the remaining 8/9 derives from the north side.
Algorithm 1 in Appendix B.2 provides the code to apply such a cosine correction to the direct normal irradiance.

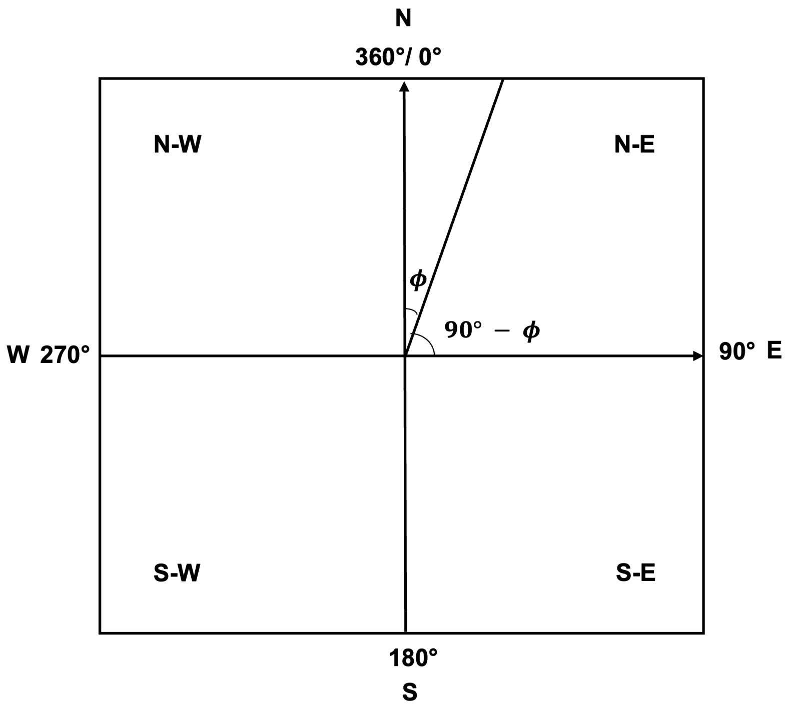

Figure 7: Weighing according to solar azimuth angle ϕ.

Laboratory

To verify the manufacturer's cosine response and to get better angular resolution, the cosine response of the EKO-711 detector has been measured in the NOAA CUCF laboratory using a 300 Watt Xenon arc lamp. The cosine response of the EKO MS-711 is measured for every wavelength pixel and every degree, both for the East-West and North-South orientations (E-W and N-S respectively).
As shown by Figure 8, both the global and diffuse signals are measured, the second one by means of a blocking disk. Subtracting the latter from the former, the direct component is then obtained.

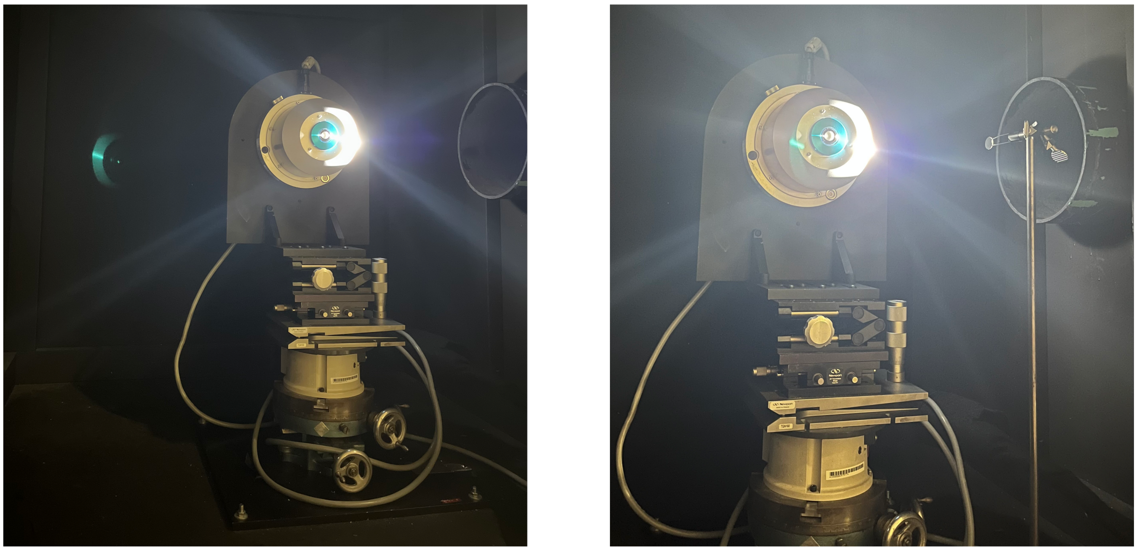

Figure 8: Left: global measurement. Right: diffuse measurement. An East-West scan with shutter open is running, i.e. daytime conditions are simulated.

Not only daytime conditions are simulated (*shutter open*), but also the dark signal[3] is considered (*shutter closed*). For every angle, 3 dark scans and 4 signal scans are made[4], the mean value is computed and the net signal is derived. This entire procedure is repeated 4 times, both for global and diffuse measurement (2), E-W and N-S orientations (2), leading to $(3 + 4) \cdot 4 \cdot 2 \cdot 2 = 112$ individual scans. Each of these measurements consists of 180 scans, each degree between -90° and 90° Θ, with a constant exposure time of 1600 milliseconds each. This leads to a measurement time of approximately 9 hours, 4.5 for each axis. Considering that the routine to save the data and the rotation from one angle to the other is time-consuming, the measuring time increases further and consists of approximately 12 hours per axis.
Additionally, note that after 8 hours of continuous operation the Xenon arc lamp shows a decay in the intensity of about 1%, which manifests itself in an increased fluctuation in the signal amplitude. After the E-W measurement has been completed, it is therefore necessary to shut down the lamp and let it cool off before analyzing the N-S axis.

Equation 10 is used to retrieve an independent cosine correction for E-W and N-S axes at every degree. Unlike the manufacturer's data processing approach, it is not necessary or even convenient to fit an equation to the data to derive a correction curve. Instead, a simple linear interpolation between angles is used to obtain the cosine correction value for any azimuth angle. Lastly, Algorithm 1 (cfr. Figure 7) can be used to partition the error and get the total correction at any given time of the day.

[3] Cfr. Section 4.1.4

[4] First a dark scan, followed by two signal scans, then another dark, again two signal scans and a final dark scan.

This measurement technique assumes that the source beam is well collimated. Since the goal of the cosine response measurement is to try to assess the instrument's performance under sunlight, the source beam is not collimated - by design. At the Earth's orbit the solar image subtends an angle of about 30 arc minutes (0.5°), and the Poynting vectors[5] at any point in the beam will fall within a 30 arc minute cone around the beam propagation vector. At the NOAA laboratory, the system is set up to produce a source beam that has a 30 arc minute divergence, simulating the sun's natural spread.
Another assumption made is that the source beam has a constant uniform irradiance pattern at any point in the beam cross-section. Since the arc lamp does not fulfil this requirement[6], it is necessary to take several scans. In fact, a fluctuation in radiance is unlikely to be repeated at the same point in a specific time interval. By averaging the values of all the scans performed, a set of reliable results can be obtained.

[5]Vector quantity representing the amount of irradiance carried by electromagnetic radiation.
[6]Halogen lamps have a much better radiant stability compared to arc lamps, but they are not as high in radiant flux (Watts/m^2) and they also drop in intensity faster.

4.2 AOD-retrieval method

To ensure a successful AOD retrieval, a procedure to calibrate the instrument has to be established. The following Section provides a comprehensive overview of the AOD-retrieval method used in this work. DNI values processed as described in Section 4.1 are considered, using both manufacturer's and laboratory-measured cosine correction.

4.2.1 Calibration

The first step of the AOD-retrieval method is to consider the linearized form of the Beer-Lambert law, described by Equation 11. Note that from now on in the work the denotation V_λ will be used instead of I_λ (or DNI_λ), respectively $V_{\lambda 0}$ instead of $I_{\lambda 0}$ ($DNI_{\lambda 0}$). The use of this notation denotes that voltage measurements, and not irradiance, will be used. Calibration factors that convert measured voltage to irradiance are not available for either the MFRSR or the EKO MS-711 channels, and they are not even necessary, because the constant would have to be applied to both sides of the equation, and thus it would cancel out.

$$ln(V_\lambda) = ln(V_{\lambda 0}) - m \cdot \sum \tau(\lambda) \tag{11}$$

From Equation 11 it is possible to produce calibration Langley plots, as shown in Figure 9. In such a graph, the slope of the natural logarithm of the measured[7] normal signal at the surface $\ln(V_\lambda)$ versus the path length m at different times of the day, is the total optical depth $\sum \tau(\lambda)$, i.e. the sum of all the contributions that attenuate the beam (cfr. Equation 2).

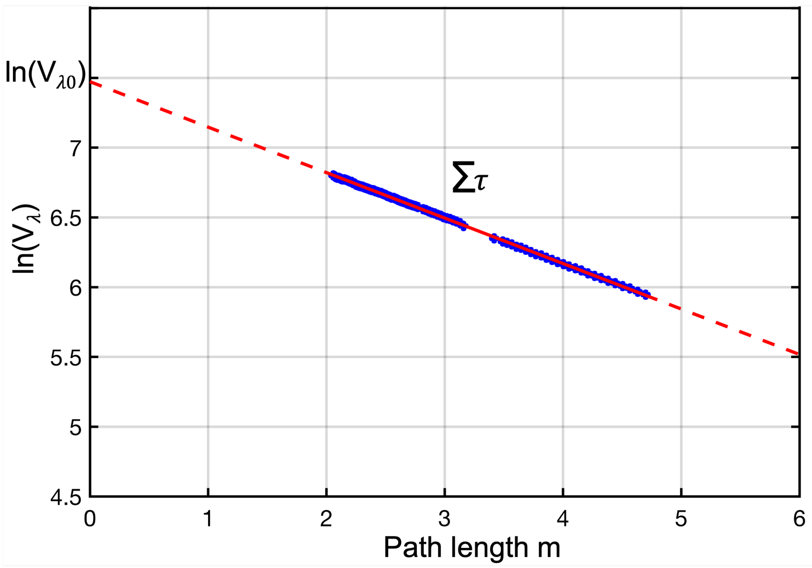

Figure 9: Langley plot, i.e. plot of the log of voltage measurements versus the path length m. A straight line is obtained if all the measurements are collected with a clear view of the sun.

The Langley plot technique allows the extrapolation of the zero path length signal $V_{\lambda 0}$ for each day, i.e. what the instrument would measure at TOA (Shaw 1983). This $V_{\lambda 0}$ value is the calibration value for the period of this plot, and can be combined with any cloud-free measurement within a few days of this calibration day to compute total optical depth τ, and AOD after Rayleigh and other contributors are removed. An absolute calibration against standard references is therefore not necessary for the AOD application (NOAA 2023).

Equation 12 provides a good estimate for the computation of path length accounting for curvature effects (Smith III and Smith 1972).

[7] More precisely, DNI is a quantity calculated from measured values of GHI and DHI, see Section 4.1.4.

$$m = \frac{1}{cos(\Theta) + 0.50572 \cdot (96.07995 - \Theta)^{-1.6364}} \tag{12}$$

The Langley calibration method is only useful when clear-sky periods are considered. A key step is therefore to eliminate data points associated with the presence of clouds to avoid interference with the Langley fit and, consequently, with the accuracy of the interpolated value at the top of the atmosphere. By using the broadband total and diffuse shortwave irradiance measurements and the known characteristics of typical clear-sky irradiance time series, the visible clear-sky detection method (Long and Ackerman 2000) allows identification of clear-sky and non-hazy periods[8].
In order to apply the Langley calibration method exactly, two other considerations must be made:

1. It has been empirically demonstrated that only values corresponding to path lengths in the range 2 - 5 produce reliable Langley plots (J. J. Michalsky, Schlemmer, et al. 2001). According to Equation 12, this approximately corresponds to solar zenith angles between 60° and 78.5°.

2. A distinction between morning and afternoon Langley plots has to be made. Generally, the amount of aerosol is higher in the afternoon, as they start to build up due to the increased turbulence associated with the building of the daytime boundary layer, and with solar-driven photochemical processes (Augustine, Cornwall, et al. 2003). As an example, Figure 10 shows how in the afternoon, as the aerosols form, the diffuse radiation increases. Simultaneously, DNI exhibits a non-symmetrical decrease with more pronounced fluctuations. Thus, concerning the Langley plots, a higher slope is expected in the afternoon compared to the morning.

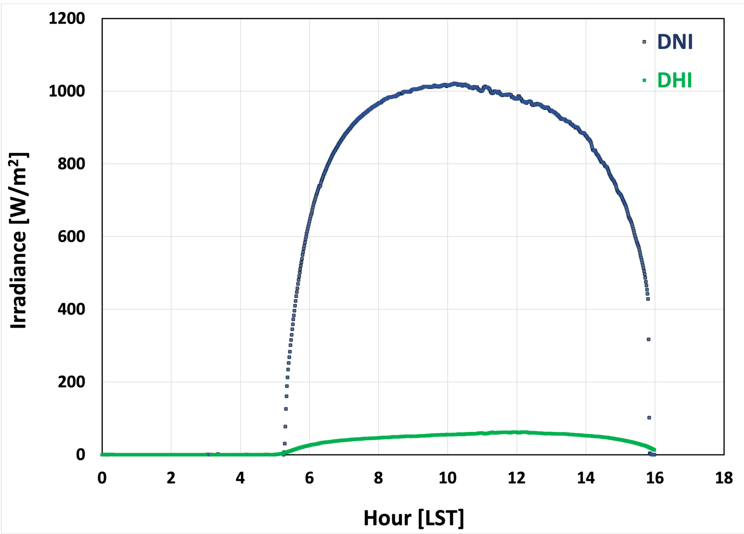

Figure 10: Direct normal (blue) and diffuse horizontal (green) irradiances at Table Mt., 20 October 2023. Shown is the non-symmetrical behavior of DNI between morning and afternoon.

For each day considered, the calculated DNI must therefore be filtered for clear-sky conditions, solar zenith angles between 62-78.5°, and separated into morning and afternoon values. Consistent with the approach adopted for the MFRSR, only one-minute datasets containing at least 75 DNI values[9] are used to produce Langley plots.
The logarithm of the normal direct signals are plotted against the corresponding airmass values. In order to exclude outliers and improve the quality of the extrapolated $V_{\lambda 0}$ value, a statistical analysis consisting of 2 steps is be performed (Augustine, Hodges, Dutton, et al. 2008):

[8] The algorithm for visible and infrared clear-sky detection is today known as RadFlux.
[9] 75 data points is an arbitrary value chosen to have sufficient measurements to provide a reliable result.

1. For each clear-sky day, a linear regression is fitted to the initial data sample. Points that lie at a distance greater than 1 standard deviation away from the regression line are considered outliers and removed from the dataset.

2. A second regression line is fitted to the new data sample. Now, points that are beyond 1.5 standard deviation from this regression line are excluded. This second screening is done in case the initial data set has a large outlier.

The final data sample is now ready for generating Langley calibrations. A linear fit of the surviving calibration Langley points allows extrapolation to zero air mass, which is the calibration value $\ln(V_{\lambda 0})$, and so the calibration value $V_{\lambda 0}$ can be computed.
The entire procedure described so far is performed independently for each of the 4 channels.

Once all the $\ln(V_{\lambda 0})$ and thus $V_{\lambda 0}$ values have been extrapolated, it is necessary to consider the variation of the earth-sun distance over the year, i.e. to correct the data with a function that normalizes the elliptical $V_{\lambda 0}$ to a circular orbit. This is done by applying Equation 13.

$$V_{\lambda 0,\text{ circular}} = \frac{V_{\lambda 0,\text{ elliptical}}}{e_0} \tag{13}$$

where
$e_0 = 1.00011 + (0.034221 \cdot cos(\gamma)) + (0.00128 \cdot sin(\gamma)) + (0.000719 \cdot cos(2 \cdot \gamma)) + (0.000077 \cdot sin(2\gamma))$

$\gamma = \frac{2 \cdot \pi \cdot (\text{day of year} - 1)}{365}$

For each channel, a V_0 time series is created by plotting all the corrected $V_{0,\text{ circular}}$ against the corresponding day of the year. The overall objective is to derive a function enabling the interpolation of $V_{\lambda 0}$ for each day of the time period analyzed, and not only for the days for which a Langley plot was explicitly generated. To achieve this, once again, it is imperative to perform a rigorous statistical analysis to derive a highly accurate function. Analogous to how it is done for the MFRSR, this consists of 2 steps (Augustine, Hodges, Dutton, et al. 2008):

1. A linear fit is applied to the time series of V_0s over the analyzed period. Values lying more than 1 standard deviation from the fit are excluded.

2. The remaining data points undergo a linear fit, and values deviating by more than 1.5 standard deviations from the refined mean are rejected.

For each channel, the final accepted $V_{0,\text{circular}}$ time series is subjected to a linear fit. This function, which describes the variation of $V_{0,\text{circular}}$ over a specific period throughout the year, enables interpolation of the top of atmosphere signal to any day within the period of the V_0 time series. Before retrieving the AOD, the interpolated daily $V_{\lambda 0}$ values have to be corrected from circular orbit back to the actual value for the day being analyzed. This is done by rearranging Equation 13, as shown by Equation 14.

$$V_{\lambda 0,\text{ elliptical}} = V_{\lambda 0,\text{ circular}} \cdot e_0 \tag{14}$$

The Langley calibration method described in this Section also allows compution of the total optical depth error. This is shown by Equation 15 (J. J. Michalsky, Schlemmer, et al. 2001).

$$\Delta\tau_\lambda = \frac{\sigma V_{\lambda 0}}{m \cdot \bar{V}_{\lambda 0}} \tag{15}$$

where
$\sigma V_{\lambda 0}$ is the standard deviation of the $V_{\lambda 0}$ values, $\bar{V}_{\lambda 0}$ the mean of $V_{\lambda 0}$ and m the airmass.
Assuming m = 1, i.e. $\Theta = 0°$, one can compute the maximum τ error for each wavelength channel.

4.2.2 AOD retrieval

Once $V_{\lambda 0}$ calibrations have been determined for clear-sky days within a certain period, they can be used to interpolate calibration V_0s for each measurement wavelength to each day within that period to retrieve aerosol optical depth.

By recalling the linearized form of the Beer-Lambert law (cfr. Equation 11) and rearranging it, an expression for the total optical depth can be obtained, as described by Equation 16.

$$\sum \tau = \frac{ln(V_{\lambda 0}) - ln(V_\lambda)}{m} \tag{16}$$

As can be deduced from Equation 2 and as explicitly shown by Equation 17, the effect of the molecular scattering and the absorption of the atmospheric gases can be removed from the total optical depth to achieve aerosol optical depth τ_a.

$$\tau_a(\lambda) = \sum \tau - (\tau_R(\lambda) + \tau_{O_3}(\lambda) + \tau_{O_2}(\lambda) + \tau_{NO_2}(\lambda) + \tau_{H_2O}(\lambda)) \tag{17}$$

Combining Equation 16 with Equation 17 yields Equation 18, a comprehensive expression for AOD.

$$AOD = \tau_a(\lambda) = \frac{ln(V_{\lambda 0}) - ln(V_\lambda)}{m} - \tau_R(\lambda) - \tau_{O_3}(\lambda) - \tau_{O_2}(\lambda) - \tau_{NO_2}(\lambda) - \tau_{H_2O}(\lambda) \tag{18}$$

Table 4 shows the spectral correction to be made for the AOD retrieval for the 4 channels of interest. Only ozone and Rayleigh scattering play an appreciable role, i.e. the contributions of O_2, NO_2 and H_2O are negligible ($< 1\%$) (NOAA 2023). This leads to the simplified version of Equation 18.

$$AOD = \tau_a(\lambda) = \frac{ln(V_{\lambda 0}) - ln(V_\lambda)}{m} - \tau_R(\lambda) - \tau_{O_3}(\lambda) \tag{19}$$

The contribution of the molecular scattering is expressed through Equation 20 (Augustine, Cornwall, et al. 2003), where λ represents the wavelength of the measurements (in μm), p the minute station pressure (hPa) and p_0 = 1013.25 hPa the mean sea level pressure.

$$\tau_R(\lambda) = 0.0088 \cdot (\lambda^{-4.15 + 0.2 \cdot \lambda}) \cdot \frac{p}{p_0} \tag{20}$$

Optical depth associated with ozone absorption τ_{O_3} can be calculated with the help of Equation 21 (Vignola, Michalsky, and Stoffel 2019).

$$\tau_{O_3}(\lambda) = \frac{O3_{measured}}{1000} \cdot \mu_{O_3}(\lambda) \tag{21}$$

where $O3_{measured}$ is the daily ozone column in Dobson Units (DU) measured by OMI satellite (please consult the website: `https://www.esrl.noaa.gov/gmd/grad/neubrew/SatO3Datatimeseries.jsp`)[10] and $\mu_{O_3}(\lambda)$ is the absorption coefficient for the ozone (mm^{-1}) based on each particular central measurement wavelength. Table 7 reports the ozone absorption coefficients at the analyzed 4 central wavelengths.

Table 7: Ozone absorption coefficients at a given central wavelength.

Wavelength [nm]	Ozone absorption coefficient [mm^{-1}]
415	0.0003
499	0.0295
674	0.0409
868	0.0013

[10] The website provides interpolated ozone data for a particular site.

Equations 19, 20 and 21 allow AOD retrievals for each day and each wavelength of interest.

Last, a cloud-screening of daily AOD time series is achieved by testing the stability of AOD (Augustine, Hodges, Dutton, et al. 2008). Selecting a moving 15-minute window[11] within the time series allows identification of clouds in a 2-step process. Initially, AOD values that deviate more than 0.05 from their neighbors are considered clouds and therefore excluded. The second step consists in fitting a Lowess curve to the time window, computing the difference between every point and the fit and removing the points based on a variable tolerance. The threshold is scaled directly by the magnitude of the central AOD within the window. High AOD values are given more tolerance than lower ones, since they are subject to more variations than backgroud aerosol. For instance, a tolerance of ± 0.02 from the Lowess fit is acceptable for AOD = 0.2, whereas for AOD = 0.014 a ± 0.01 variation is allowed (ibid.).

As a reference, an aerosol optical depth of 0.01 at 500 nm corresponds to an extremely clean atmosphere, whereas a AOD equal to 0.4 at the same wavelength would describe very hazy conditions. In the U.S. average aerosol optical depth values at 500 nm varies from 0.1 to 0.15 (NOAA 2023). Another general characteristic is that for the same aerosol concentrations, AOD decreases as the sampling wavelength becomes larger (Mohr and Holland 2023).

4.2.3 Ängstrom exponent

A measure to characterize the wavelength dependence of AOD is provided by the Ängstrom exponent α (Eck et al. 1999). This unitless number, which also provides information on the relative size of the aerosols present in the vertical column, is the slope of the logarithm of AOD versus the logarithm of wavelength λ, as illustrated by Equation 22.

$$\alpha = -\frac{\ln(AOD_{\lambda_1}) - \ln(AOD_{\lambda_2})}{\ln(\lambda_1) - \ln(\lambda_2)} \tag{22}$$

where λ is the wavelength in μm.
The Ängstrom coefficient exhibits an inverse correlation with the average size of the aerosol particles: the larger the aerosols, the smaller the exponent. Values greater than 1 indicate a dominance of fine particles (such as smoke and industrial pollution), whereas numbers below 1 suggest an optical prevalence of coarse particles (such as dust, ash, and sea spray) (Mohr and Holland 2023; Liu et al. 2018). Cloud droplets and cirrus ice particles are usually large (radius $\sim 5\ \mu$m) and so α is very small (nearly zero).
Thus, spectral measurements at various wavelengths can be used to infer aerosol properties.
As α represents the slope of ln(AOD) versus ln(λ), its value should remain constant for any pair of channels employed for its computation. To be consistent with the procedure followed for MFRSR AOD processing, the 868 nm and 499 nm channels are used to compute the Ängstrom exponent.

4.3 MFRSR AOD retrieval

The AOD retrieval-method outlined in Section 4.2 has already been applied to the data collected by the MFRSR instrument installed at Table Mt. Hence, Langley plots, V_0 time series and daily AOD values are used in this work for comparison with the data obtained by EKO MS-711. It is important to note that data obtained from the MFRSR instrument account for shading correction, as well as for its own cosine response measured in the laboratory.

[11] A 15-minute time window is chosen and then incrementally shifted by one minute, and the analysis are iteratively applied.

5 Results

The results presented in this Section refer to data collected by EKO MS-711 at Table Mt. during September-October 2023. More precisely, data from September 20th to October 28th have been analyzed. The absence of analysis for days before September 20th is mostly due to instrument malfunctions (or non-optimal measurements). Two other days, namely October 11th and October 14th, have been excluded because of overcast conditions (in which aerosol measurements would have lacked of significance) and the occurrence of a solar eclipse, respectively.
This two-month period has been chosen for the following reasons:

- Stable operation of the EKO MS-711, that has just been installed at Table Mt. in May 2023.
- A considerable number of clear-sky days, generating a large number of Langley plots thus enhancing the robustness of the generated V_0 function.
- Same calibration period as the MFRSR.

5.1 AOD retrieval

The AOD-retrieval method (cfr. Section 4.2) enables computation of AOD for the period of data collected. The same procedure is applied to four differently processed EKO MS-711 DNI datasets, to each of which the shading correction described in Section 4.1.2 has been applied:

- Raw data (neither slit nor cosine correction);
- Slit correction (no cosine correction);
- Slit + cosine correction (manufacturer);
- Slit + cosine correction (NOAA laboratory);

Subsequently, these EKO MS-711 AOD values are compared with each other and with the ones retrieved by the MFRSR, in order to understand the relationship between the two instruments.

A first comparison is made between AOD calculated from raw CCD single cell data (i.e., not slit corrected) and AOD derived from slit-corrected DNI. Figure 11 shows the results for an exemplary day (September 27th) for the 499 nm channel. The results for the 3 remaining channels are reported in Figure C1 in Appendix C.

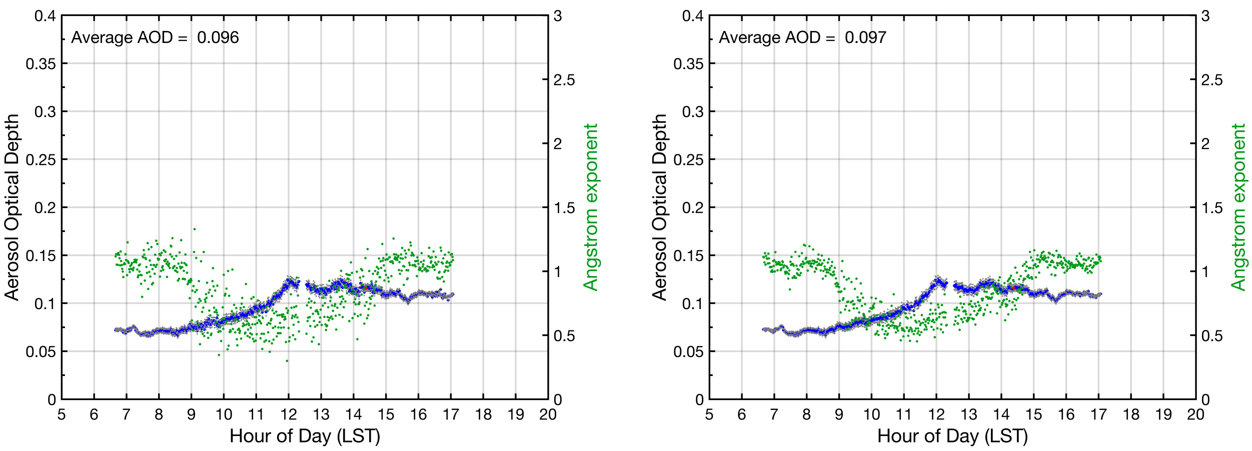

(a) Raw data **(b)** Slit correction

Figure 11: AOD for the 499 nm channel, September 27th, 2023. In blue are represented the points that have passed cloud screening, in red those rejected, and in green the Ängstrom exponent. Gray dots indicate the range of the AOD error.

No significant difference in terms of mean daily value is observed. However, the AOD retrieved from DNI to which a slit correction has been applied show a greater robustness. This is particularly clear in the reduction of the noise in the Ängstrom exponent (green dots).
For this reason, slit-corrected data are preferred to single-cell raw data and from now on used in this work.

The second step tests whether the application of the cosine correction improves the data in terms of robustness and agreement with MFRSR AOD. Both manufacturer's and NOAA's cosine correction are applied independently to the slit-corrected data. Figure 12 shows the comparison between slit-corrected data only (Figure 12a), AOD computed by considering manufacturer's and NOAA's cosine correction (Figure 12b and 12c respectively) and the AOD retrieved from the MFRSR (Figure 12d). Again, the results for the 499 nm channel for September 27th, 2023 are reported.

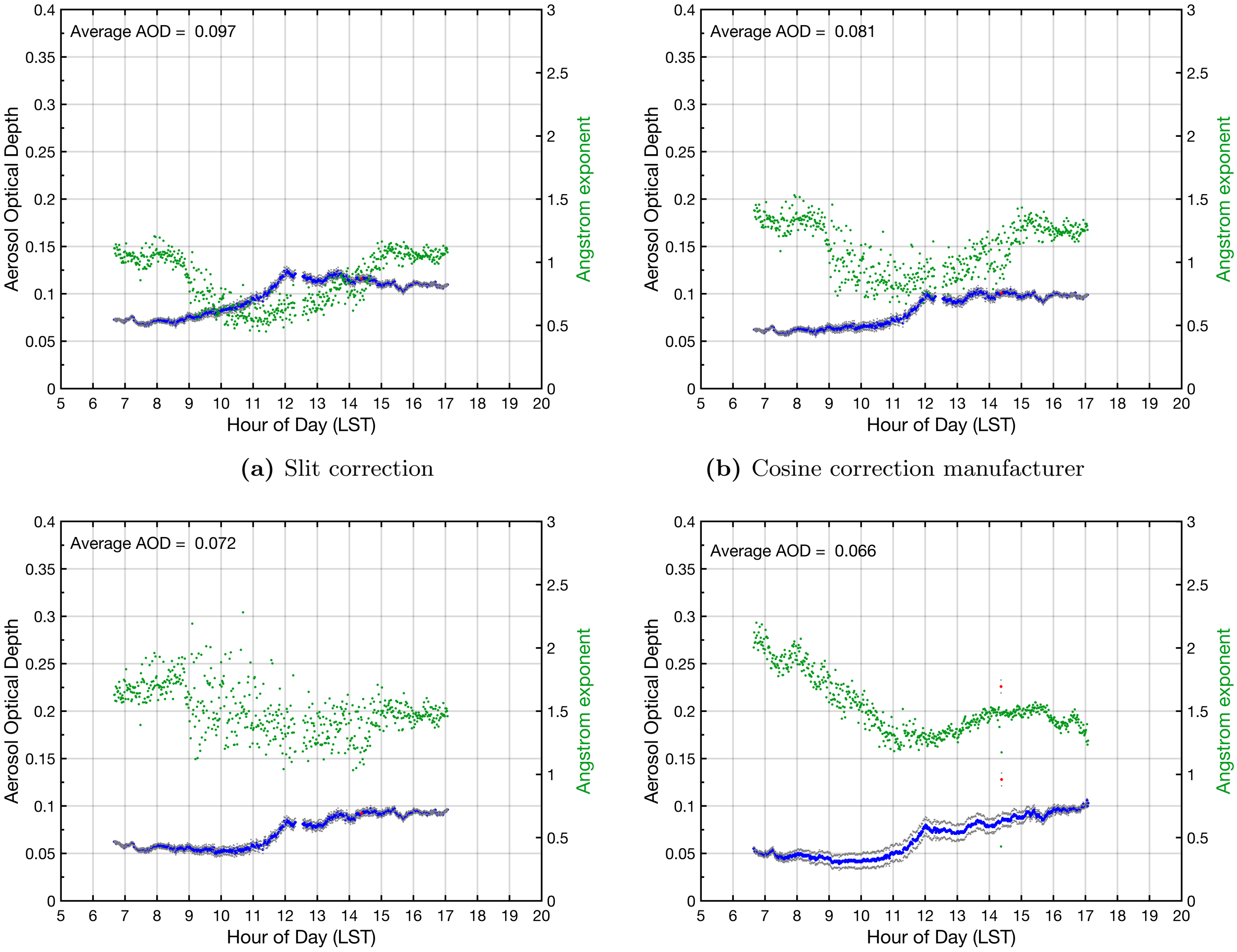

(a) Slit correction

(b) Cosine correction manufacturer

(c) Cosine correction NOAA laboratory

(d) MFRSR

Figure 12: AOD for the 499 nm channel, September 27th, 2023. In blue are represented the points that have passed cloud screening, in red those rejected, and in green the Ängstrom exponent. Gray dots indicate the range of the AOD error.

A notable drop in the mean daily AOD can be observed when applying the manufacturer's cosine correction to the slit-corrected data. The decrease in AOD when using *our* cosine correction is even more significant (for this particular case daily mean AOD from 0.097 to 0.072, corresponding to a

26% decrease), and it leads to the best agreement with the MFRSR (daily mean AOD = 0.066). Also note that the AOD error - represented by the range between the gray dots - is significantly higher for the MFRSR compared to the EKO MS-711.
Regarding the Ängstrom exponent, the situation is somewhat more intricate. Indeed, the noise increases at every step (Figure 12a - 12c), but so does the magnitude of α, reaching values similar to those obtained with the MFRSR. It's also important to note that the pattern of α throughout the day does not align precisely with the values resulting from MFRSR measurements.

These observations - both in terms of AOD and Ängstrom exponent - are consistent across all channels and throughout every day of the analyzed period, thus suggesting that considering the actual cosine response of the instrument is indispensable. In particular, applying NOAA's cosine correction seems to have a greater impact on the results than the manufacturer's, as shown in the next Sections.

5.2 Cosine correction

Evident differences between manufacturer's and NOAA's cosine response are shown in Figure 13. As already mentioned in Section 4.1.5, EKO Instruments Co., Ltd has performed a cosine response at 10° Θ increments, while at NOAA's laboratory the measurements have been conducted at one-degree increments. In addition, the manufacturer's cosine response has been measured independently of the wavelength (red curve only), whereas *our* cosine correction is specific for every pixel of interest, i.e. the four channels. This can have big impacts on the AOD retrieval and on the Ängstrom exponent α.
In general, for higher solar zenith angles Θ, the discrepancy between measured and ideal cosine response (on the y-axis) becomes more and more pronounced. On the East-West direction the cosine response curves are quite symmetric and similar, except for the 415 nm channel, which indicates that a greater correction should be applied to the data (cfr. Figure 13a). The North-South axis shows a weaker degree of symmetry (cfr. Figure 13b), and the manufacturer's curve diverges noticeably from what has been measured in NOAA's laboratory.
Again, these observations suggest that having an accurate cosine correction measurement is essential in order to improve the quality of the AOD retrieval.

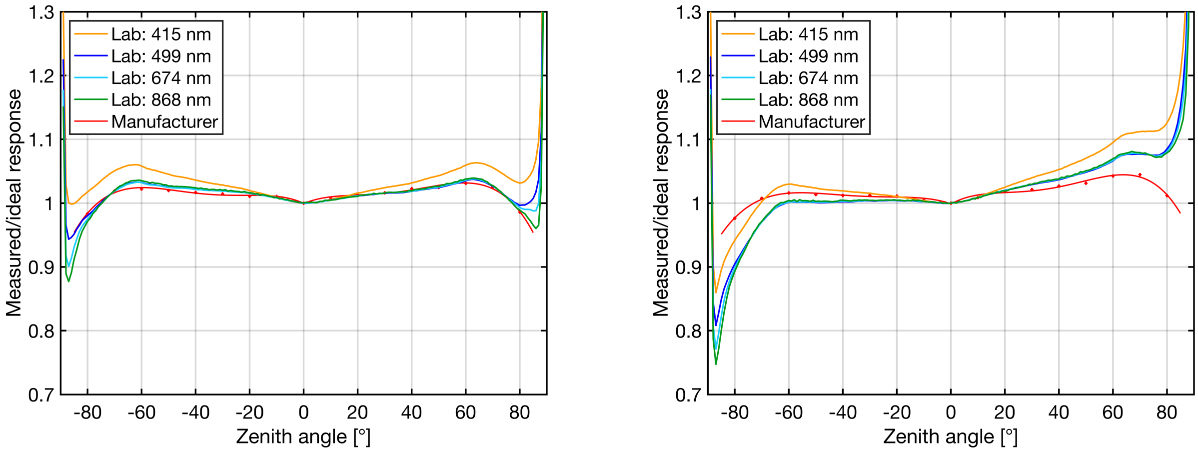

(a) E-W axis **(b)** N-S axis

Figure 13: Cosine correction, as provided by the manufacturer (red) and measured in the laboratory of NOAA (4 channels distinctly).

5.3 Comparative analysis: EKO MS-711 vs. MFRSR

To compare all of the AOD values obtained from both instruments for the analyzed period, correlation plots can be used, as illustrated by Figure 14 for all channels under consideration. The AOD retrieved from EKO MS-711 refers to slit-corrected DNI data to which NOAA's cosine correction has been applied.

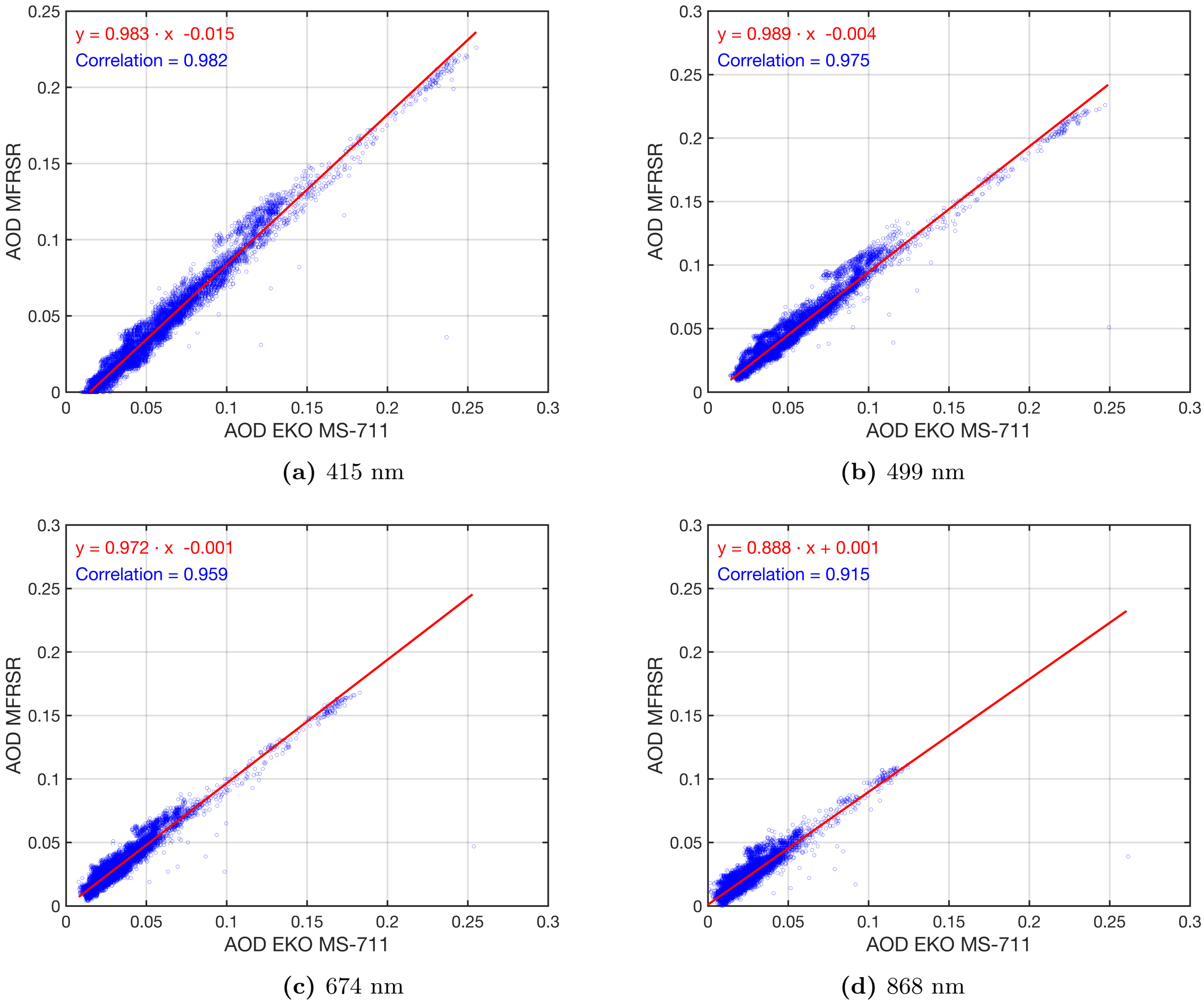

(a) 415 nm

(b) 499 nm

(c) 674 nm

(d) 868 nm

Figure 14: Correlation between AOD values retrievd from the MFRSR (y-axis) and from the EKO MS-711 (x-axis). Results for the 4 channels are presented.

The first clear result is that AOD retrieved from the EKO MS-711 is consistently greater than that retrieved from the MFRSR. The only exception is represented by the 868 nm channel for which, however, the slope of the regression line is smaller than for the other channels.
An interesting pattern can be observed: as the offset between MFRSRS and EKO MS-711 decreases at higher wavelength (from -0.015 at 415 nm to +0.001 at 868 nm), the noise amplifies, resulting in a decrease in the correlation between the two instruments (from 98.2 % at 415 nm, to 91.5 % at 868 nm).
Moreover, it is worth noting that the slope of the regression line is close to 1 for the first 3 channels, while it is 0.888 for the 868 nm channel. Combined with the previous observations, it can be concluded that this channel - which is the noisiest - exhibits the greatest variability in the results.

Figure C2 in Appendix C shows the results obtained by applying the manufacturer's cosine correction to DNI slit-corrected data acquired from EKO MS-711. Not surprisingly, consistent with the findings presented in Sections 5.1 and 5.2, the correlation between MFRSR and EKO MS-711 is poorer than that obtained using NOAA's cosine correction. The larger offset indicates that the AOD retrieved by EKO MS-711 is greater than that obtained from MFRSR. Additionally, the correlation between the two instruments decreases with wavelength, suggesting a weaker degree of matching and a greater variability in the data.
The situation worsens if slit-corrected data without any cosine correction applied are considered, as reported in Figure C3 in Appendix C. In this case, not only does the offset increase, but more importantly, the variability in the data increases significantly. Thus, the correlation not only decreases, but it also loses significance.

Hereafter, the use of data to which NOAA's cosine correction has been applied is therefore justified.

Figure 15 represents a way to look at the differences between the AOD retrieved from EKO MS-711 and MFRSR (Δ AOD = $AOD_{\text{EKO MS-711}}$ - AOD_{MFRSR}). A boxplot is illustrated for each channel, where the median value of the AOD difference (red horizontal line), the 25th and 75th quartiles (edges of the box, in blue) are represented, as well as the outliers (red dots). The black horizontal lines represent the lower and upper whiskers, corresponding approximately to the 16th and 84th quartiles, respectively.

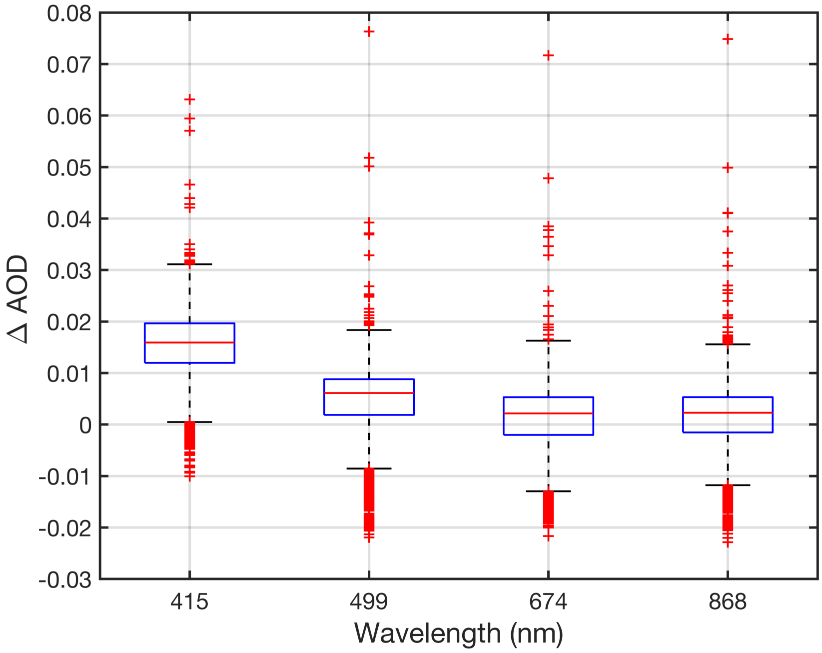

Figure 15: Difference in AOD between EKO MS-711 and MFRSR for the 4 channels.

In accordance with Figure 14, the median value of the AOD difference decreases as the wavelength increases, and this value closely resembles the offset portrayed in the correlation plots. The width of the box is similar for all 4 channels, although the 415 nm channel is shifted upward compared to the other channels. The outliers are similarly distributed upward and downward. However, it can be seen that in the negative region (i.e. when the AOD coming from MFRSR is greater than that derived from EKO MS-711) the outliers are quite dense, while in the positive region they are much more variable, with differences reaching relatively high values. Because these are outliers, and that is, single points that can be neglected, this does not solicit for further investigation.

Figure 16 reports for every channel the daily time series for both EKO MS-711 (blue, top plot) and MFRSR (red, middle plot) retrieved AOD. The green bottom plots report the AOD absolute difference Δ AOD = $AOD_{EKO\ MS\text{-}711}$ - AOD_{MFRSR}. Note that the x-axis of these plots is incremented by the day-of-year.
As already seen so far but never explicitly stated, Figure 16 clearly shows that the AOD measured in the 415 nm channel is the largest (lowest contribution of O_3), followed by 499 nm, 674 nm and 868 nm, for which Rayleigh scattering is the only correction (cfr. Table 4).
Note that day 277 (October, 4th, 2023) is the day with highest AOD detected within the period considered.

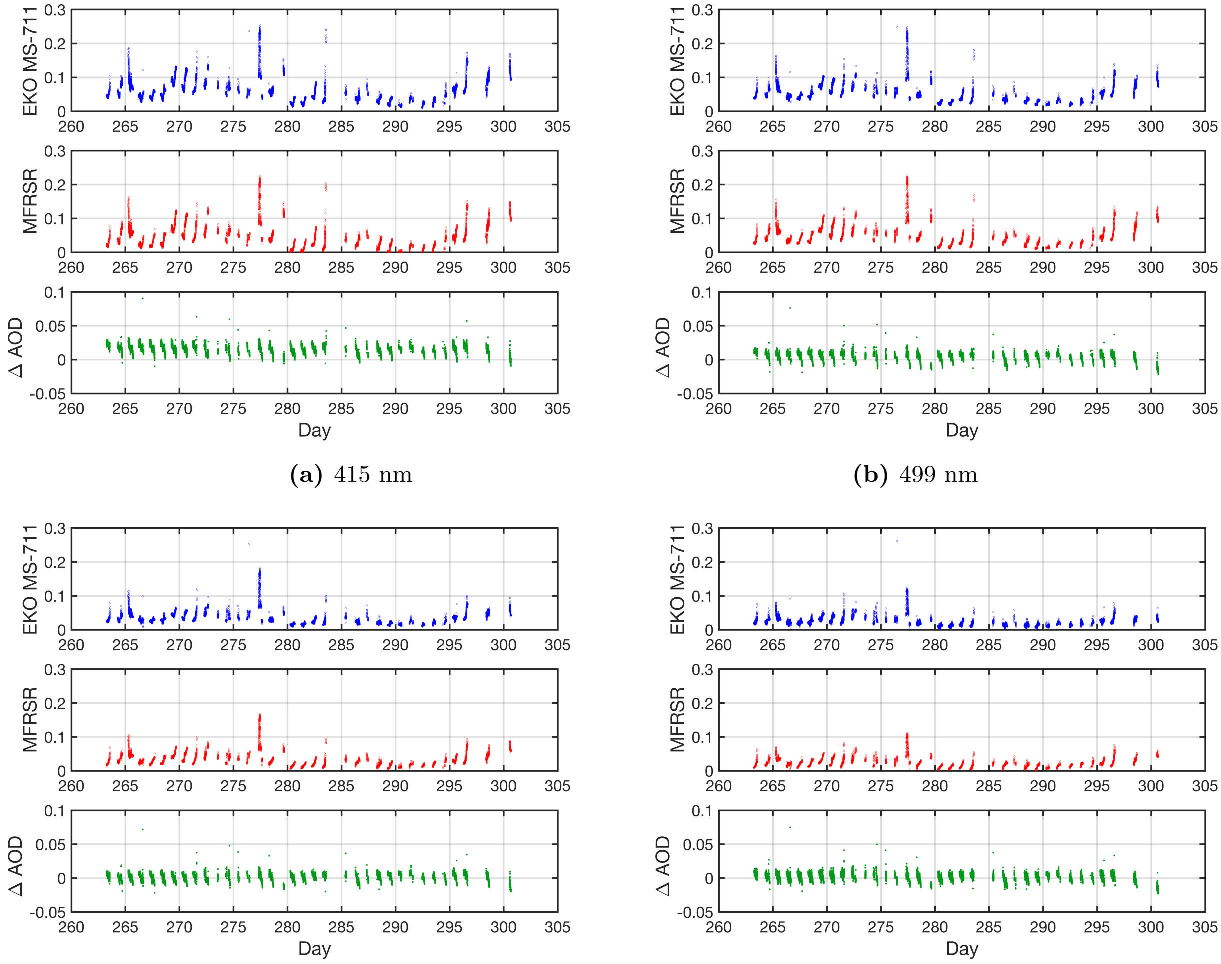

(a) 415 nm

(b) 499 nm

(c) 674 nm

(d) 868 nm

Figure 16: Daily AOD time series for EKO MS-711 (blue) and MFRSR (red). The difference in AOD (green) is also reported.

A daily pattern can clearly be observed. During the morning the AOD tends to be lower, whereas in the afternoon the concentration of aerosols in the atmosphere is typically higher. In fact, as discussed in Section 4.2.1 and shown by the non-symmetrical shape of Figure 10, aerosols start to build up in the afternoon due to the increased turbulence associated with the building of the daytime boundary layer, and with solar-driven photochemical processes.
The behavior of the two instruments is very similar, but one difference is evident. During the morning - when the AOD is lowest - the differences between the two instruments are greater. As

the concentration of aerosols increases (in the afternoon), the EKO MS-711 and MFRSR agree better and the differences are therefore smaller. Especially for the 674 and 868 nm channels, the differences in the afternoon even become negative, indicating that MFRSR-retrieved AOD is greater than EKO MS-711 AOD.

Another view of the AOD trends and differences between the two instruments is presented in Figure 17. This time, hourly AOD time series are investigated. These plots further highlight how AOD gradually increases throughout the day, whereas the difference between EKO MS-711 and MFRSR AOD tends to decrease (negative slope of the green curve).

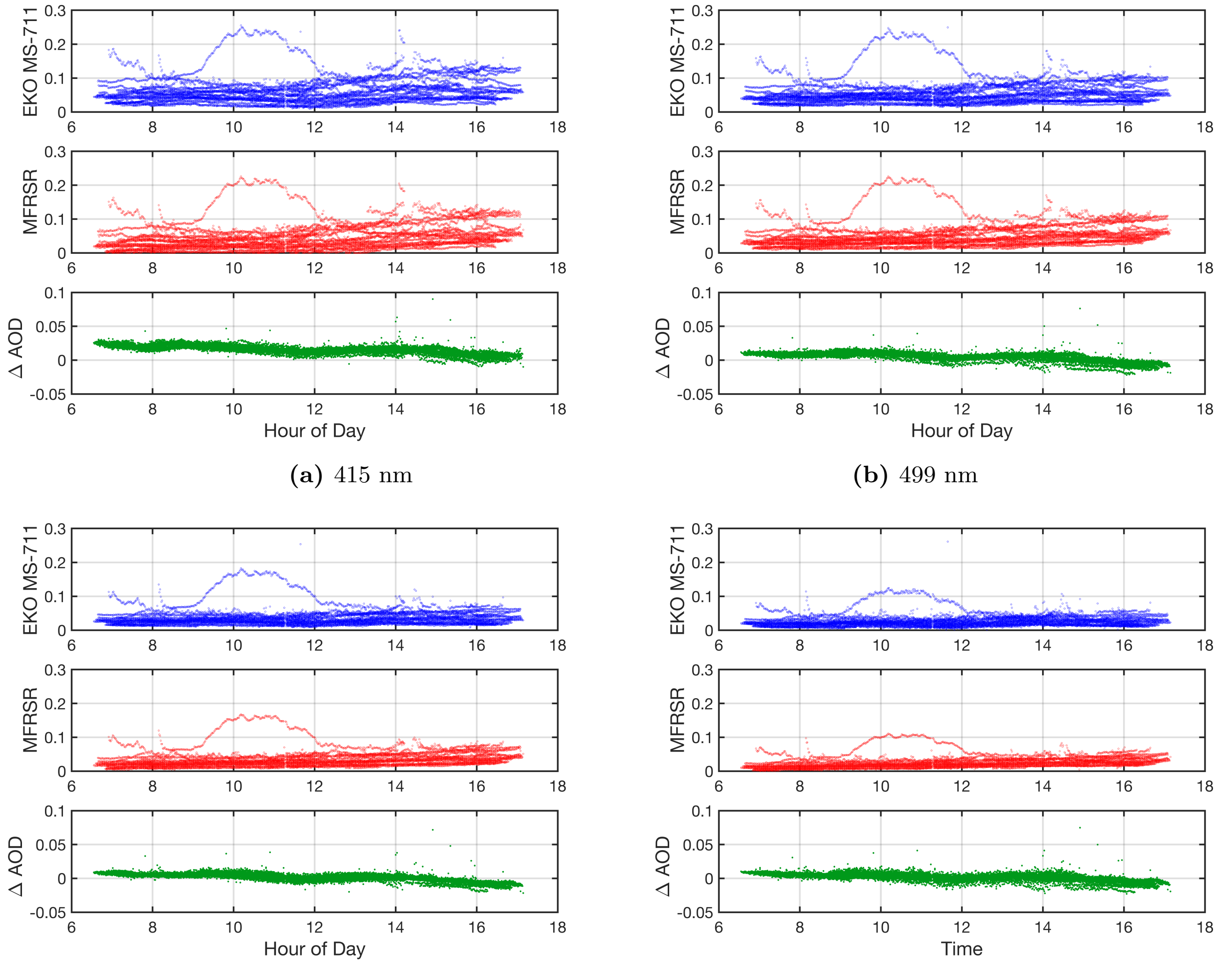

(a) 415 nm **(b)** 499 nm **(c)** 674 nm **(d)** 868 nm

Figure 17: Hourly AOD time series for EKO MS-711 (blue) and MFRSR (red). The difference in AOD (green) is also reported.

Similar observations can be made by analyzing Figure 18, where the behavior of the AOD ratio ($AOD_{MFRSR}/AOD_{EKO\ MS\text{-}711}$) with respect to the AOD retrieved from the EKO MS-711 is shown. Three main features are evident. First, the 415 nm channel exhibits the weakest agreement between the 2 instruments, displaying a pronounced asymmetry at low AOD values. Second, each channel shows improved agreement as the AOD increases, yet the ratio consistently remains below 1, indicating that AOD from the EKO MS-711 is mostly higher than that from the MFRSR. Lastly, the 868 nm channel has the highest variability, especially at low AOD values (ratio > 2).

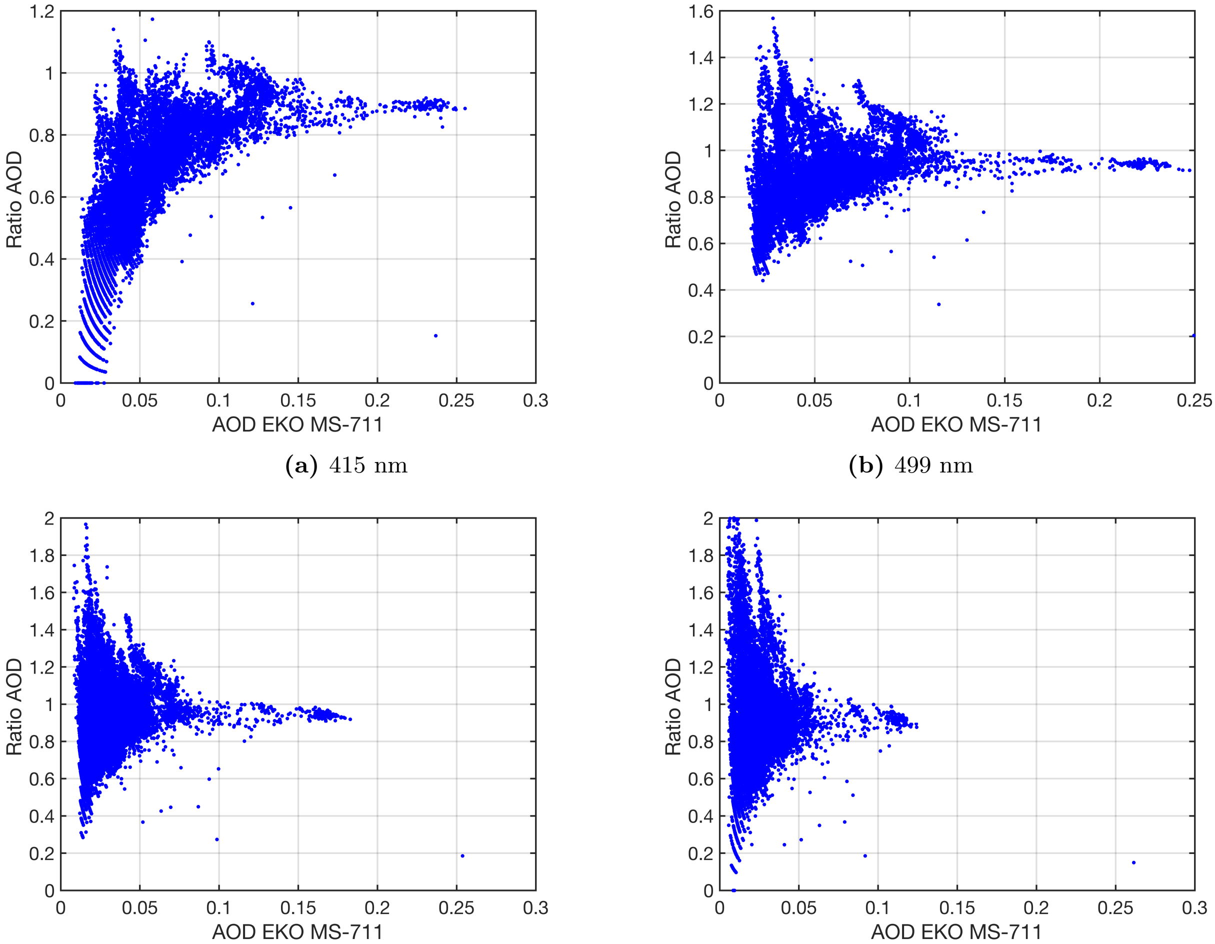

(a) 415 nm **(b)** 499 nm **(c)** 674 nm **(d)** 868 nm

Figure 18: AOD ratio (y-axis) versus AOD retrieved from EKO MS-711 (x-axis).

5.4 PMOD reference

The World Meteorological Organization (WMO), recognized in 2006 "the need for establishing a primary reference AOD Centre to satisfy the need for traceability of Optical Depth (OD) measurements, conducting international intercomparisons guaranteeing data quality needed in climate studies" (WMO 2023). The quality of AOD data from intercomparison of different instruments can be evaluated based on difference criteria, i.e. traceability is confirmed when the AOD difference between instruments or networks falls within specified limits, as reported by Equation 23 (ibid.).

$$U95 < \pm(0.005 + \frac{0.010}{m}) \tag{23}$$

where U95 represents the limit of acceptability, the first term on the right (0.005) accounts for instrumental and algorithmic (post-processing) uncertainties, while the second term represents the uncertainty related to the calibration of each instrument - that is, it is established that the relative uncertainty in instrument calibration should be 1% or less (since m represents airmass, with values ranging from 1 and above).
Every 4 years, instruments from around the world are tested at the Physikalisch-Meteorologisches Observatorium Davos, World Radiation Centre (PMOD/WRC) in Davos (Switzerland) against 3 Precision Filter Radiometer (PFR), i.e. the reference standards.

In the penultimate session (2016), NOAA sent an MFRSR to Davos to test against the standards. The results were satisfactory, i.e., the AOD retrieved from the MFRSR were within the limits established by Equation 23, and the instrument is therefore considered to be reliable for retrieving AOD.
A similar intercomparison to that performed at PMOD can therefore be carried out in this work. Here, the MFRSR is considered the standard, and comparisons are made to the EKO MS-711 using tolerances defined by PMOD. Results are shown in Figure 19, where the green points represent the difference Δ AOD = $AOD_{\text{EKO MS-711}}$ - AOD_{MFRSR} (as in Figure 17) and the red points the upper and lower limits. Note that the largest tolerances are around noon when the solar path length is the smallest.

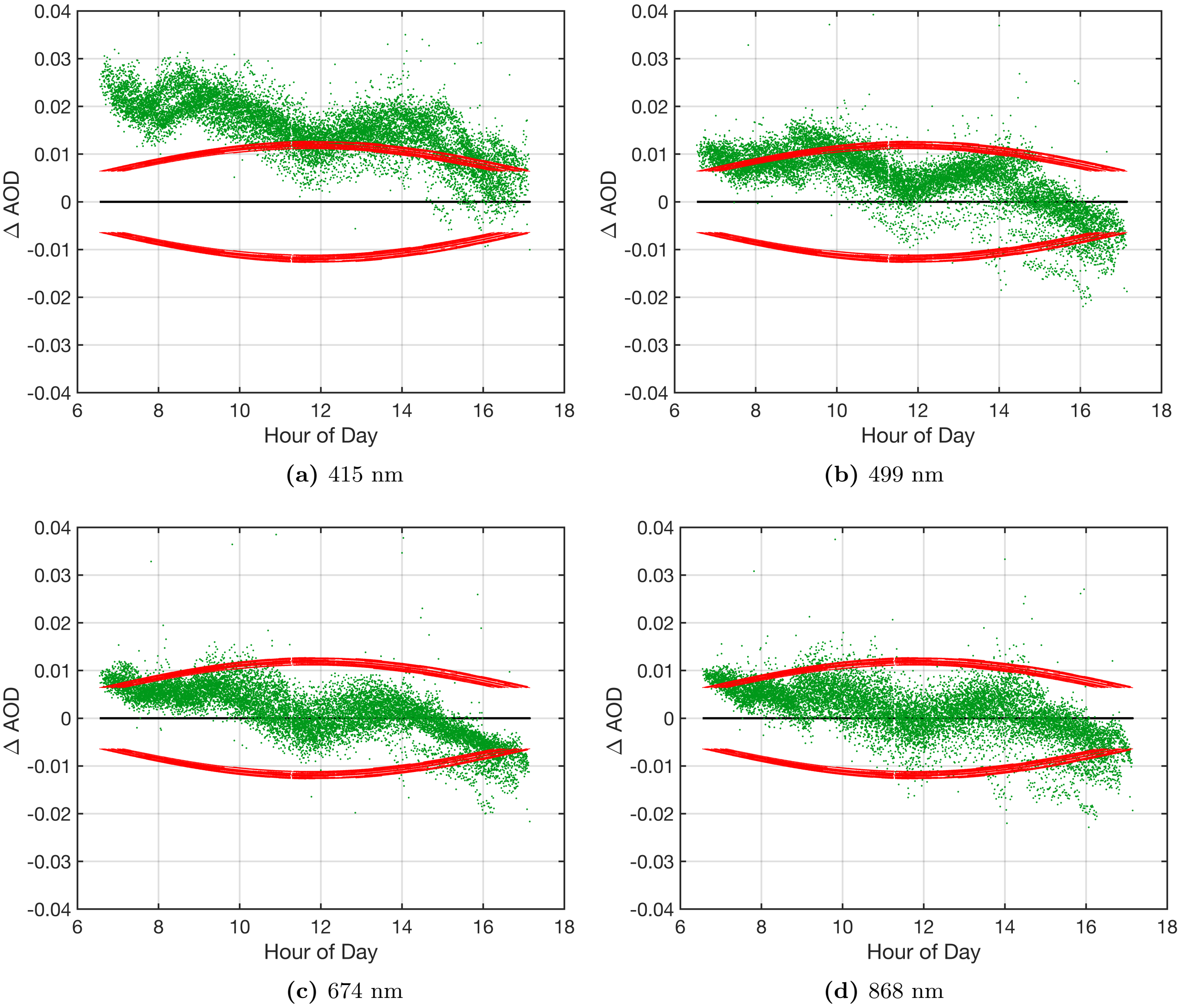

(a) 415 nm **(b)** 499 nm

(c) 674 nm **(d)** 868 nm

Figure 19: Hourly AOD difference between AOD retrieved from EKO MS-711 and MFRSR (green dots). Red points represent the limits established by PMOD/WRC.

Differences are generally outside of the PMOD limits for the 415 nm channel AODs, but are mostly acceptable for the other three channels, and the two instruments seem therefore to be comparable. Two evident and fundamental features are the tilt of the slope from morning to afternoon and the particular shape of the difference curves. This will be discussed in detail in Section 6.

5.5 Diffuse to global ratio

Scatter plots of the ratio of diffuse-to-global irradiance (DHI/GHI) for the MFRSR against the EKO MS-711 allow for a comparison of their measured quantities. Since the AOD has been retrieved for solar zenith angles Θ up to 82°, only the corresponding irradiance values are considered. Figure 20 illustrates the correlation plots for the 4 channels, as well as the equations for the regression line. The goal of this analysis is to determine whether the two instruments collect similar signals and whether any systematic bias can be observed.

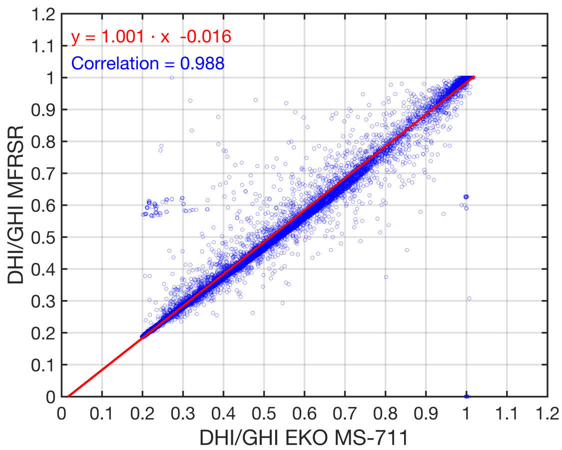

(a) 415 nm.

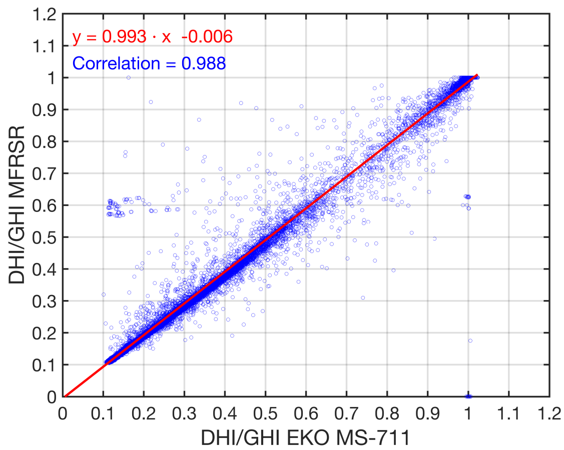

(b) 499 nm.

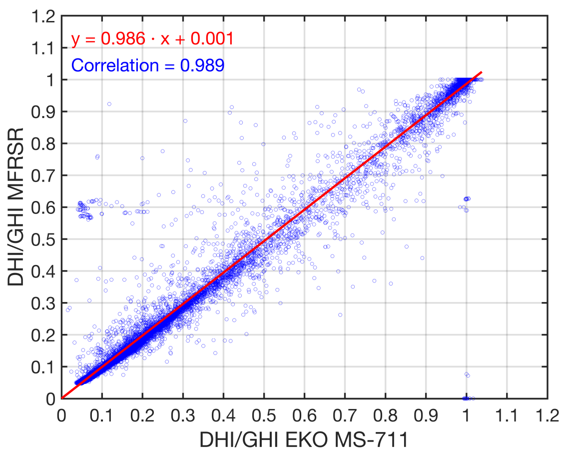

(c) 674 nm.

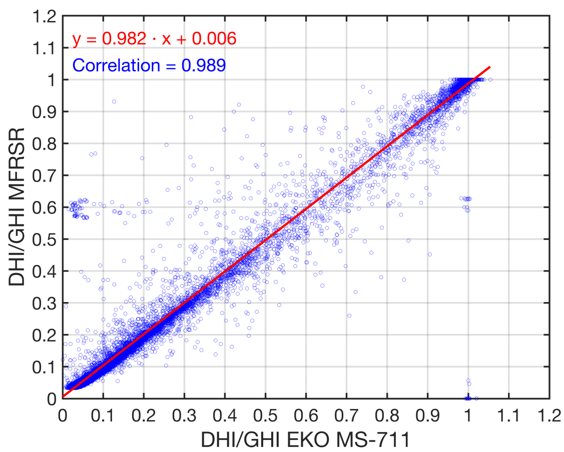

(d) 868 nm.

Figure 20: Correlation between the ratio diffuse to global (DHI/GHI) of MFRSR (y-axis) and EKO MS-711 (x-axis).

A robust correlation between MFRSR and EKO MS-711 across every channel is evident. Nevertheless, in all 4 channels an offset with similar magnitude to the one illustrated in Figure 14 can be observed, suggesting a potential influence on the AOD differences as illustrated in Figure 19.

The boxplots in Figure C4 (cfr. Appendix C) illustrate the percentage difference computed by Equation 24.

$$\text{Difference} = \frac{\text{DHI/GHI}_{\text{ MFRSR}} \text{ - } \text{DHI/GHI}_{\text{ EKO MS-711}}}{\text{DHI/GHI}_{\text{ EKO MS-711}}} \tag{24}$$

Despite the good correlation between the instruments, a notable spread can be observed, especially in the 868 nm channel. Since this channel is used to calculate the Ängstrom exponent, the wide spread may explain the noise in α shown for instance by Figure 12c. Furthermore, the negative difference in all channels indicates that the ratio of signals measured by EKO MS-711 is higher than that of MFRSR.

5.6 Calibration

Differences between the AOD retrieved from the two instruments may result from discrepancies between their Langley calibrations. It is therefore worth investigating this aspect more closely. Table C1 and Table C2 in Appendix C report the extrapolated $\ln(V_0)$ values as well as $\sum\tau$ for EKO MS-711 and MFRSR, respectively. According to the procedure described in Section 4, only clear-sky calibration Langley plots for the two-month period analyzed are considered, and a distinction between morning and afternoon has to be made.
It is therefore possible to compare the calibration Langley slopes (i.e. $\sum\tau$) of the MFRSR against those of the EKO MS-711, as illustrated by Figure C5 in Appendix C. Two populations can be clearly distinguished: blue points represent morning slopes, whereas magenta dots stand for afternoon. Not surprisingly, the latter ones are greater, as aerosols build up during the day. Regardless of the dichotomy between the slopes of morning and afternoon calibration Langley plots, theoretically, they should all point to the same calibration V_0. Since no distinctions are made between morning and afternoon for the V_0 calibration curve, it makes sense to fit a single regression line for each channel. Consistent with the AOD results, the offset is highest for the 415 nm and lowest for the 868 nm channel.
This is also shown by Figure 21, where the 4 calibration slope regression lines are presented in a single plot. Since both the Rayleigh and the ozone contributions are independent of the instrument, the total optical depth $\sum\tau$ is reflected in the AOD offset (cfr. Equation 19).

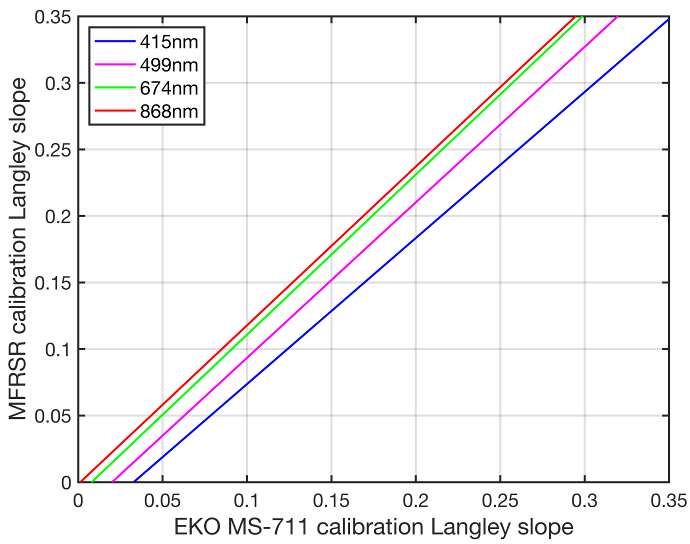

Figure 21: Calibration Langley slope regression line, MFRSR (y-axis) against EKO MS-711 (x-axis).

Figures C6, C7, C8 and C9 in Appendix C show for each channel the V_0 time series and linear fits for both MFRSR and EKO MS-711. To isolate the best Langley calibrations, those time series are subjected to a statistical elimination to remove the outliers. In Figures C6-C9, the blue points have been accepted and the red points rejected. Only the surviving blue points are subjected to the linear fit.

The equation of the linear fit and the τ error are also displayed. The linear fit is used to interpolate calibration V_0 values to any day within the two-month analysis period so that AOD calculations are possible on days when Langley calibrations are not. The Figures show that EKO MS-711 is particularly stable, i.e. the V_0 curve is more flat compared to the MFRSR, as shown by the lower slope of the regression line. This is also reflected in the error (computed according to Equation 15), significantly lower for the EKO MS-711 compared to the MFRSR[12], with a difference of approximately one order of magnitude across all channels. The absolute value of the V_0 can not be compared between the two instruments, since the signals are measured in different ways. However, it appears clear how the value of V_0 decreases as the wavelength increases.

In terms of V_0 stability, it seems that the EKO MS-711 is more robust than the MFRSR. Nevertheless, since a short two-month period is considered, the variations in the curves don't affect the results dramatically. In fact, looking at Figure 22 which shows the deviation of the V_0 values from the mean, no systematic difference between the MFRSR and EKO MS-711 can be observed. It can thus be stated that the difference in the slopes seem to outweigh differences in the V_0.

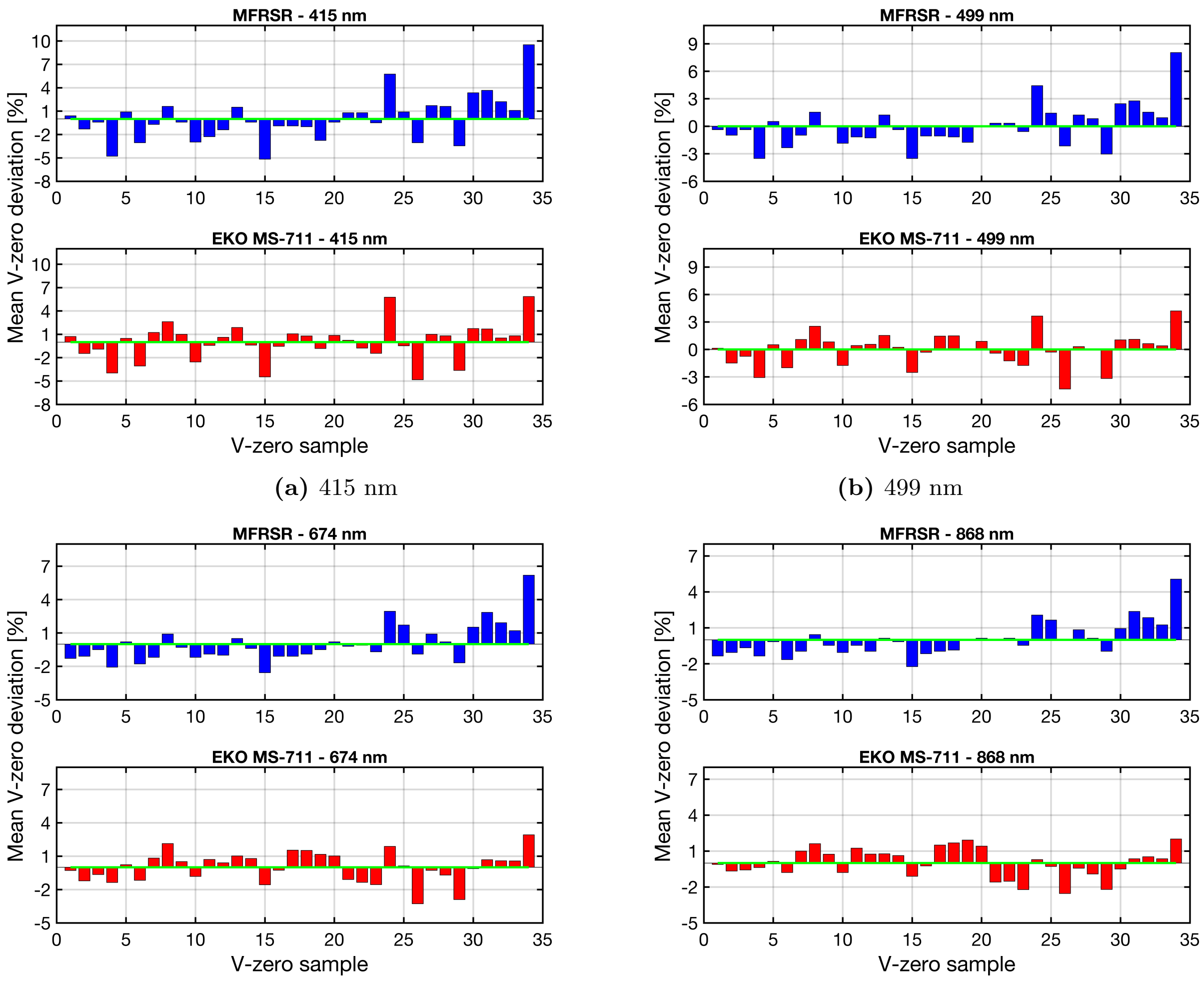

(a) 415 nm **(b)** 499 nm

(c) 674 nm **(d)** 868 nm

Figure 22: Percentage deviations from the mean V_0 value, MFRSR (blue) and EKO MS-711 (red).

[12]The greater AOD error of MFRSR is also highlighted through comparison of Figures 12c and 12d.

Last, the V_0 statistical elimination method is based on the standard deviation rejection method described in Section 4.2.1. A Gaussian behavior of the V_0 is assumed. Figure C10 in Appendix C shows the frequency distribution of the V_0 values for the EKO MS-711. Although the distributions are slightly skewed and not perfectly Gaussian, the results seem to justify the use of this method.

5.7 Ängstrom exponent

To test the AOD wavelength dependence for both instruments, the logarithm of AOD versus the logarithm of wavelength (cfr. Equation 22) can be computed. A representative example for the sample is depicted in Figure 23, which illustrates this comparison for a single data point, September 27th, at noon.
Since AOD measured by EKO MS-711 is mostly greater than the one retrieved from the MFRSR, the blue curve lies higher than the red one. The slope of the two curves are of similar magnitude, indicating that the Ängstrom exponent α for the two instruments are comparable. A higher degree of linearity, and therefore a smaller variability in α, can be seen in the MFRSR compared to the EKO MS-711 curve. Even though the 415 nm channel in the MFRSR seems to be misaligned, the Ängstrom exponent calculation is not affected, as the 868 nm and 499 nm channels have been used throughout the work. However, as shown more robustly by Figure C11 in Appendix C, the systematic nature of this offset can highlight some inaccuracies in the AOD retrieval for this channel. In contrast, EKO MS-711 seems to show variability in the 868 nm channel and thus in α, therefore exhibiting a greater noise in α.

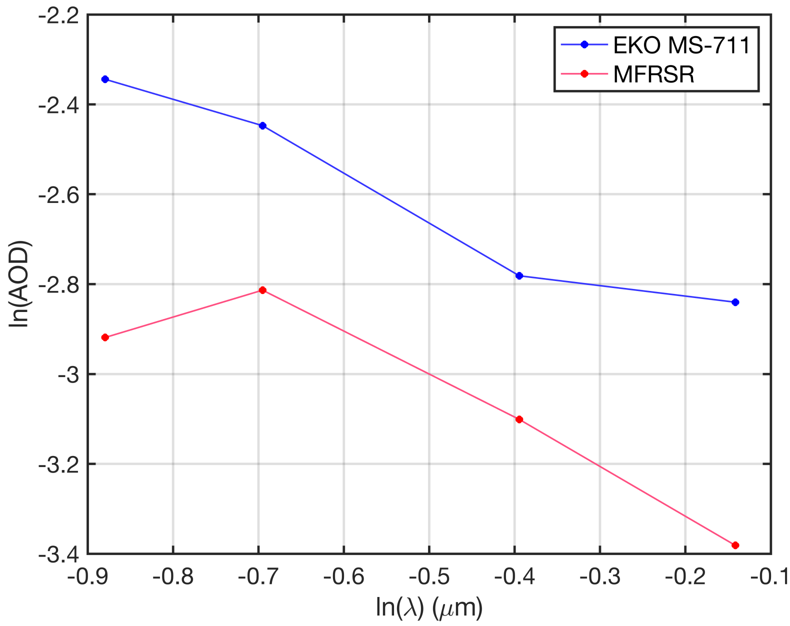

Figure 23: Logarithm of AOD versus logarithm of wavelength. The slope of the two curves represent the Ängstrom exponent α.

A comparison between the two instruments in terms of α correlation is shown by Figure 24, where two ways to compute the exponent are represented. Blue data correspond to the 499-868 nm channels used in this work, whereas the 499-674 nm combination serves as a comparison.
Figure 24 indicates that the Ängstrom exponent of EKO MS-711 is usually greater than that of the MFRSR. However, given the considerable variability especially from α values > 1, it is difficult

to make a clear statement.
The data period is dominated by continental aerosols, as illustrated by the large prevalence of α values between 1 and 2, whereas coarser particles as dust ($\alpha < 1$) and smoke ($\alpha \geq 2$) are present to a lesser extent.
Lastly, no extreme difference between the two alternatives can be noticed, except for the fact that the first combination (499-868 nm) yields greater variability even at lower α values (α EKO MS-711 $\approx$ 0.3 - 0.8), whereas the spread at higher α is of similar magnitude.

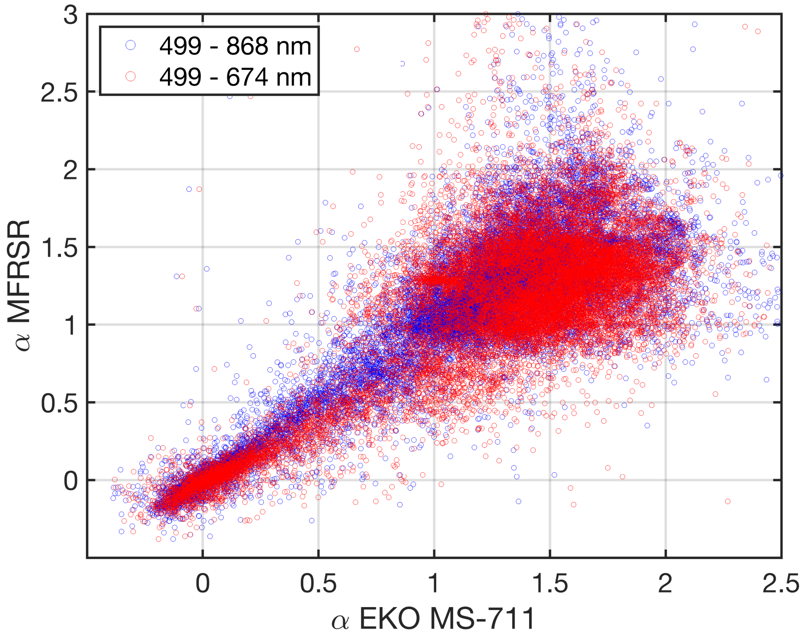

Figure 24: Scatter plot of MFRSR Ängstrom exponent versus EKO MS-711 Ängstrom exponent, computed in two ways, using the 499 and 868 nm channels (blue) and the 499 and 674 nm channels (red).

6 Discussion

6.1 AOD comparison

In terms of mean daily AOD, it has been shown that applying a slit correction leads to an improvement of the data quality (cfr. Figure 11). In fact, since the FWHM of the dispersion grating in the EKO-711 is 7 nm, the wavelengths in the immediate vicinity of the central channels considered also play a key role, and must therefore be taken into account by considering a weighed Gaussian distribution. By doing that, more robust (i.e. less noisy) results are obtained.
A further improvement is reached if a cosine correction is also applied to the DNI data. By considering the internal features of the instrument and so the deviations from an ideal cosine response, an improvement in the mean daily AOD has been observed, as shown by Figure 12. In particular, the cosine correction measured at NOAA is more accurate than the one provided by the manufacturer, since a wavelength dependence is considered and single degree increments are performed. With regard to the EKO MS-711, having cosine response information at 10° Θ intervals supplied by the manufacturer was found to be unsatisfactory. However, comparing the AOD computed using the NOAA cosine correction (Figure 14) with that using the EKO MS-711 cosine correction (Figure C2) clearly shows that AOD computed with NOAA's cosine corrected EKO MS-711 data compares better with MFRSR AOD, both in terms of a stronger correlation and a smaller offset. These results are consistent for the 4 channels and therefore justify the use of NOAA's cosine corrected data for the majority of the work.
Generally, EKO-711-computed AOD is greater than MFRSR AOD. Some interesting features can also be noted. First, the difference is greatest for the 415 channel. Second, a diurnal cycle in the differences shows the largest discrepancy in the morning (when AOD is generally lowest) and smaller differences in the afternoon, when the AOD start building up. Last, a strong variability by low AOD values dominate in particular at 868 nm.
By taking MFRSR as a reference and using the procedure follwed at PMOD/WRC, the agreement between the two instruments has been assessed in terms of quality. Except for the 415 nm channel, for which the AOD differences are too large to ensure a good comparability between the two instruments, EKO MS-711 retrieved AOD falls mostly within the limits of acceptability.
However, two main features are evident:

- The shape of the AOD differences resemble the one of the cosine correction curve shown by Figure 13. This suggests the high sensitivity of the data to the cosine correction function being applied, and therefore the crucial importance of an accurate cosine measurement.

- Differences between the EKO MS-711 and MFRSR AOD are greater in the morning than in the afternoon. To investigate that discrepancy, the levelling of the two instruments has been checked, and a tilting of the MFRSR towards South-East has been discovered. Such an inclination results in an erroneously high DNI measurement. This implies that less attenuation of the solar beam is considered, therefore resulting in a lower AOD than the one retrieved from the EKO MS-711. The differences between the two instruments should therefore be smaller in the morning and, analogously, slightly larger in the afternoon. By levelling the MFRSR it is therefore expected that the AOD differences will fall even better within the limits of acceptability set by the PMOD/WRC, in particular in the morning, where the calculated differences are currently too high.

6.2 Diffuse-to-global ratio and V_0 calibration comparisons

Three possible reasons for the discrepancies in the AOD retrieved from the two instruments have been identified, namely differences in the diffuse-to-global ratio (Figure 20), in the calibration Langley slopes (Figure C5) and in the V_0 calibration time series (Figures C6 - C9).
Similar to the AOD comparisons between the two instruments, the diffuse to global ratio irradiance comparison is quite robust. Nevertheless, a considerable variability in the 868 nm channel is present, as well as significant offset in the 415 nm.

As shown by the AOD error derived from the scatter in the V_0 calibration time series over the analysis period (Figures C6 – C9 in Appendix C), the EKO MS-711 seems to be more stable than the MFRSR. In Figure C5, calibration Langley slopes ($\sum\tau$) of the EKO MS-711 exhibit consistently greater values than the MFRSR. These findings suggest that differences in the slopes outweigh differences in the V_0 stability.
It seems reasonable to assume that the tilt of the MFRSR towards the S-E direction is one of the main causes for both the ratio and calibration slope offset. However, this does not explain either the high variability especially at 868 nm, nor the fact that the offset at 415 nm is far greater than that of the other channels.

6.3 Ängstrom exponent

By looking closely at the Ängstrom exponent α, it is possible to make a few remarks. First, the MFRSR shows a particular behavior in the 415 nm channel, which is systematically misaligned with respect to the other channels. This has led to further investigation regarding the behavior of the MFRSR. From an analysis of the data over the past years, one result has emerged: beginning on September 15^{th}, 2022, the 415 nm channel of the MFRSR has begun to measure incorrectly. This is demonstrated by the lower AOD values compared to the 499 nm channel (when, instead, it should be higher, as aerosols scatter more at shorter wavelengths). The causes of this discrepancy are still unclear, but they could be attributed to a lost transmission in diode or filters in the 415 nm channel, due to natural events or internal problems in the instrument. This evidence may therefore explain the higher offset in the 415 nm channel, because the 415 nm AOD retrieved from the MFRSR is expected to be greater, and the differences with that from the EKO MS-711 therefore level off. This again shows the importance of continuously monitoring also the MFRSR, which has been taken as the standard in the absence of other instruments at Table Mt. but which, itself, presents challenges.
Since α is inversely related to the size of aerosol particles (the larger the aerosol, the smaller the exponent), it can also be concluded that over the period of data analyzed, the presence of fine particles has been dominant, whereas days with coarser particles ($\alpha < 1$) have rarely occurred.

6.4 Uncertainties

Some clear sources of uncertainty and error that have afflicted this work can be recognized.
First, both instruments have shown evident issues. Being a relatively new instrument, the EKO MS-711 still has some challenges that need to be solved. In fact, the first version of the software NAMI presented bugs, jamming from time to time and so leading to a restart of the computer, thus interrupting continuous measurement. Another structural problem has involved the rotating shadow band, which occasionally has appeared to be out of position and needed its mounting screws tightened. Since the instrument was installed at Table Mt. and not at the NOAA building, 15 km to the south, daily monitoring was not possible, and the above problems have often been detected without knowing exactly when they occurred. This has led to unreliable DHI and GHI data and is the main reason for the short data period. A new version of the software was released in January 2024 (NAMI 2.0), with the fixing of bugs and other improvements that should improve the data reliability.
The analysis in the NOAA laboratory also revealed another interesting aspect of the EKO MS-711. As shown by Figure 25, the assembly holding the white diffuser is pushed off to the North-West side of the instrument shell (cfr. Figure 3, it is not installed for the cosine measurement in laboratory[13]). This means that the diffuser is off axis to the dome in the same direction, thus partially obstructing the collected signal and having direct consequences on its quality. Note that a dome can be optically neutral in an assembly only when all the components are centered along the dome's symmetry axis (zenith or z-axis).

[13]The white shield can be removed during laboratory measurement since, being elevated, it has no effect on albedo or reflection.

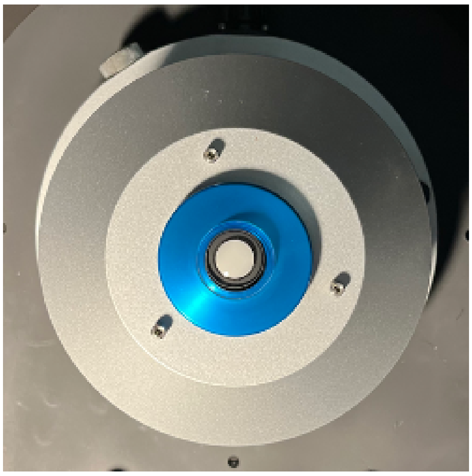

Figure 25: Picture of the EKO MS-711 taken at the NOAA laboratory.

Moreover, looking closely at Figure 3 highlights that during the side band and diffuse measurements, the blue collar around the dome and the white part of the sun shield next to the blue collar are bright and may be a source of scattered light error. This error should be accounted for in the cosine correction, but it still represents a source of uncertainty.

Regarding the MFRSR, two main problems have been highlighted, namely, the fact that the instrument was not levelled and the malfunction of the 415 nm channel. These two uncertainties have profound consequences on the results. The former can be easily solved with a closer monitoring, while the latter needs more careful analysis in the laboratory. In addition, this work has made use of the MFRSR cosine response measured in 2015. A measurement in January 2024 of this MFRSR cosine response has shown no particular differences from the one used in this work. Therefore, a way to eliminate the effects of MFRSR tilting could also be to perform a kind of relative cosine response between the two instruments, that is, to find a correction for the EKO MS-711 based on the mutual behavior of the signals measured by the two instruments. However, this method is based on data, and consequently an independent measurement of the cosine response is preferred. Lastly, it should be pointed out that the configurations of the two instruments are different and so are their measurement principles. While the MFRSR is a filter-based instrument, the EKO MS-711 is spectroradiometer (dome-instrument) which measures in the wavelength range 300-1100 nm. The two instruments are therefore not necessarily expected to behave in the same way.

Uncertainties also arise from the procedure chosen to retrieve AOD (cfr. Section 4.2). Choosing datasets containing at least 75 DNI values for the generation of calibration Langley plots is arbitrary and it is justified simply for purposes of consistency with the MFRSR. However, it might be worthwhile to see if significant changes can be found by considering, for instance, 50 or 100 DNI values.
The statistical analysis for the $V_{\lambda 0}$ (applied two times) consists of 2 steps, and an arbitrary threshold of 1 standard deviation is chosen in the first screening. Some variations of this method can be considered, such as including a third rejection step and changing for instance the initial value $\sigma = 0.8$, that is to impose a stricter condition at the beginning.
All these options seem to be equally valid, and no choice appears better than another. It follows that the V_0 function obtained may exhibit variations that are more or less significant depending on arbitrarily imposed values. A sensitivity analysis could help to better investigate this aspect. However, for the small sample of data used in this research, one would not expect large differences in the V_0 calibration time series by applying the variations suggested above.

As already mentioned, the data period itself is a source of uncertainty. In fact, the period analyzed has been particularly clean, resulting in low average daily AOD values (constantly < 0.1 at 499 nm, except for October, 4$^{\text{th}}$). These conditions may be surprising, as such small AOD values are typically associated with winter conditions, when AOD tends to be at its lowest - as opposed to summer, when it tends to be the highest (Augustine, Hodges, Dutton, et al. 2008). However, the period analyzed lies between summer and winter. These low AOD values are more difficult to detect compared to smoke conditions, where the AOD is high. This statement is supported by the fact that the best agreement between the two instruments is in the afternoon, when the AOD builds up and increases in the atmosphere (cfr. Figure 19). It should also be noted that this large variability at low AOD can be misleading, as the relative differences may be large (for instance +100%) but, since these values are still extremely low, the absolute differences are conversely not so significant. The large scatter at low AOD can also explain the variability of the Ängstrom exponent for fine particles ($\alpha > 1$).

6.5 Further steps

Several adjustments and enhancements can be implemented to attain more robust and stable results, and therefore a more reliable comparison.
First, it is desirable that the problems related to RSB will be solved, as well as it is expected that the new NAMI 2.0 software will fix the bugs present in the previous version. Besides that, as the EKO MS-711 is still a relatively young instrument, so many unknowns that need to be clarified are still present. Problems related to MFRSR must also necessarily be corrected, namely the strange behavior in the 415 nm channel must be better investigated and the tilt toward S-E encountered during the analyzed data period must be corrected.
In the future it is desirable to perform a measurement campaign involving other instruments in order to validate the results more strongly. Such a procedure has already been attempted in this work, taking as an additional reference the AERONET station located at Neon, about 7 km from Table Mt. (and thus at very similar latitudes and longitudes). At this NASA station the AOD is retrieved from a sun photometer pointing towards the sun, unlike the EKO MS-711 and the MFRSR, which are shadow band instruments. However, as shown by Figure 26 for the 499 nm channel, the comparison between the three instruments is difficult to interpret.

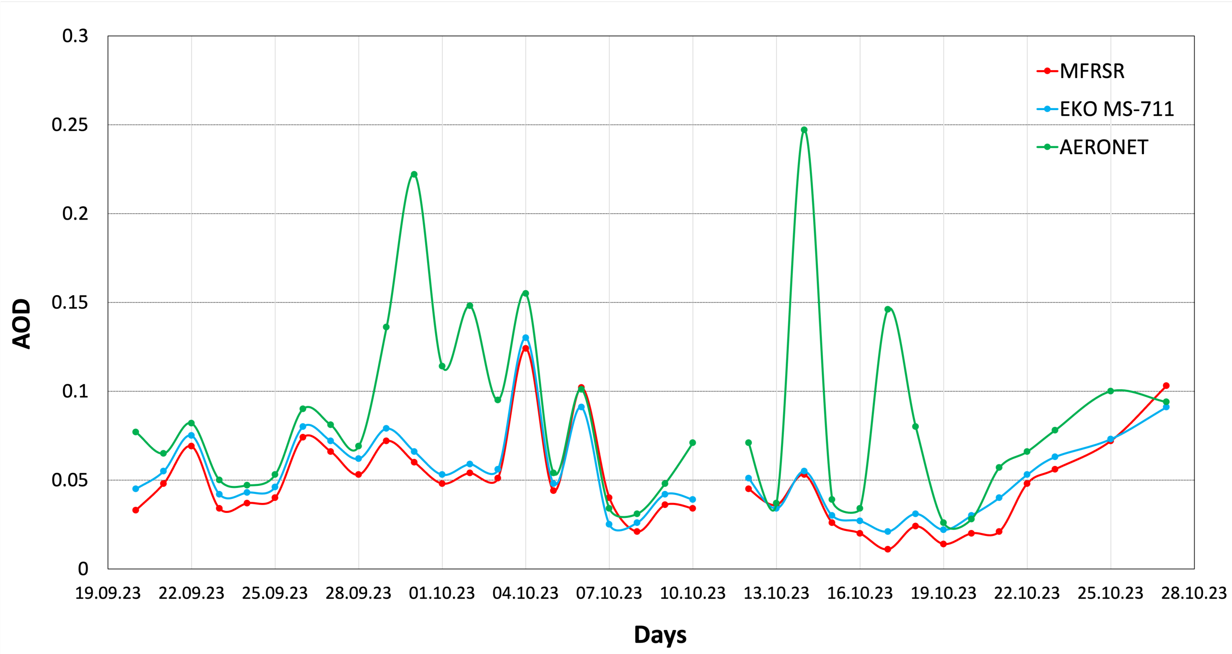

Figure 26: AOD at 499 nm retrieved at Table Mt. by the MFRSR (red) and the EKO MS-711 (blue) compared to the retrieval at Neon from a sun photometer (green).

The Neon station is located in a valley at an elevation about 150 meters lower than Table Mt. Since high concentrations of aerosols are typically in the lower layers - thus leading to high AOD -, it is therefore expected that this difference in elevation may contribute to a AOD discrepancy between the instruments. In addition, that station is located about 4 km from Longmont Airport, and this almost certainly explains the peaks shown in Figure 26. On one hand, this comparison resembles the variability one might expect at such a station, but on the other hand it does not provide any added value to the validation of the results. Therefore, it would be beneficial to perform a comparison between various instruments, operating on different principles, located at the same location.

In the future a longer measurement campaign with several collocated sun photometer instruments, including the EKO MS-711 should be conducted. First, this would allow an evaluation of the long-term performance and behavior of the EKO MS-711, and second an investigation of periods of high and low AOD.
Moreover, similar to what was done in Figure 23, being a spectral instrument, the EKO MS-711 provides the ability to generate Ängstrom exponent plots for several wavelengths, in order to have more robust results and possibly recognize trends and problems. This would also allow a deeper investigation of other channels. Note that the wavelength-dependent absorption contamination would have to be considered and removed from all channels used in such an analysis.

Such an approach could certainly lead to establishing the quality of the EKO MS-711 and possibly using it as a standard for AOD retrieval in the future.

7 Conclusion

The comparison between EKO MS-711-derived AOD and MFRSR-retrieved AOD at MFRSR wavelengths has shown a satisfactory degree of correlation, although some systematic deviations have been detected. In particular, it has been seen that the 868 nm channel is the one with the greatest variability - and thus noise -, whereas the 415 nm channel has the greatest mismatch. In fact, the 415 nm channel is the only one falling outside the acceptability limits set by PMOD/WRC (considering MFRSR as the standard instrument). This comparison also reveals the importance of an accurate cosine error measurement - which can not be renounced - on the AOD retrieval and, in general, the need of a good characterization of the instrument. In this regard, note that by making use of the cosine curve measured at NOAA the AOD differences with the MFRSR have been halved compared to those measured with the cosine correction curve provided by the manufacturer.

The reasons for these discrepancies have been investigated, and some interesting results have emerged. Inaccuracies in the MFRSR have been highlighted, namely a malfunction in the 415 nm channel and a tilting of the instrument towards the South-East direction. The comparison of the ratio *diffuse to global* irradiance for both instruments has shown results consistent with the AOD. The same applies for the calibration Langley slope comparison. From one side, it seems to be reasonable to assume that the tilting of the MFRSR towards S-E direction is one of the main reasons responsible for both ratio and calibration slope offset, and so for the differences in AOD. On the other hand, these differences may also arise due to the different operating principle of the instruments (filter-based vs. dome-instrument) or due to the internal characteristics of the devices.

In addition to the problems just mentioned, some other uncertainties have affected this work, as the selected procedure for the AOD retrieval. The malfunction of the NAMI software and the RSB of the EKO MS-711 have also been an obstacle to continuous data measurement. Moreover, the short data period with low AOD values has made the comparison more difficult, leading to great variability, and prevented testing operation under atmospheric conditions with higher loads. This is a source of further uncertainty.

In light of these considerations, in the current state it appears difficult to think of replacing existing distinct-channel sun photometers such as the MFRSR with the EKO MS-711. Too many unknowns and too many uncertainties are still present. However, a potential in the EKO MS-711 has been identified and a transition in the future does not seem to be inconceivable. Appropriate studies and improvements are crucial and indispensable, as well as a long-term large-scale measurement campaigns under varying atmospheric conditions involving several instruments. This approach would facilitate a more robust comparison and possibly make the transition plausible. At this stage, if the performance of the EKO MS-711 were to be clarified and accepted, the possibility of more continuous information would be real, thus broadening the horizons of research. Other components, such as water vapor or sulphur dioxide, could for instance be better investigated.

References

Arola, A. et al. (2022). "Aerosol effects on clouds are concealed by natural cloud heterogeneity and satellite retrieval errors". In: *Nature Communications* 13.7357. DOI: https://doi.org/10.1038/s41467-022-34948-5.

Augustine, J. A., C. R. Cornwall, et al. (2003). "An Automated Method of MFRSR Calibration for Aerosol Optical Depth Analysis with Application to an Asian Dust Outbreak over the United States". In: *Journal of Applied Meteorology* 42.2, pp. 266–278. DOI: https://doi.org/10.1175/1520-0450(2003)042<0266:AAMOMC>2.0.CO;2. URL: https://journals.ametsoc.org/view/journals/apme/42/2/1520-0450_2003_042_0266_aamomc_2.0.co_2.xml.

Augustine, J. A., J. J. DeLuisi, and C. N. Long (2000). "SURFRAD–A National Surface Radiation Budget Network for Atmospheric Research". In: *Bulletin of the American Meteorological Society* 81.10, pp. 2341–2358. DOI: https://doi.org/10.1175/1520-0477(2000)081<2341:SANSRB>2.3.CO;2. URL: https://journals.ametsoc.org/view/journals/bams/81/10/1520-0477_2000_081_2341_sansrb_2_3_co_2.xml.

Augustine, J. A., G. B. Hodges, C. R. Cornwall, et al. (2005). "An Update on SURFRAD—The GCOS Surface Radiation Budget Network for the Continental United States". In: *Journal of Atmospheric and Oceanic Technology* 22.10, pp. 1460–1472. DOI: https://doi.org/10.1175/JTECH1806.1. URL: https://journals.ametsoc.org/view/journals/atot/22/10/jtech1806_1.xml.

Augustine, J. A., G. B. Hodges, E. G. Dutton, et al. (2008). "An aerosol optical depth climatology for NOAA's national surface radiation budget network (SURFRAD)". In: *Journal of Geophysical Research: Atmospheres* 113.D11. DOI: https://doi.org/10.1029/2007JD009504. URL: https://agupubs.onlinelibrary.wiley.com/doi/abs/10.1029/2007JD009504.

Babb, D. (2023). *The Roads Traveled Most By Radiation.* URL: https://www.e-education.psu.edu/meteo3/l2_p4.html.

Benniston, A. et al. (2014). "The Quest for Highly Fluorescent Chromophores: An Evaluation of 1H,3H-Isochromeno[6,5,4-mna]xanthene-1,3-dione (CXD)". In: *RSC Adv.* 4. DOI: 10.1039/C4RA09728A.

CO, EKO Instruments (2016). *MS-711N Spectroradiometer.* URL: https://www.eko-instruments.com/in/categories/products/spectroradiometers/ms-711n-spectroradiometer.

Eck, T. F. et al. (1999). "Wavelength dependence of the optical depth of biomass burning, urban, and desert dust aerosols". In: *Journal of Geophysical Research: Atmospheres* 104.D24, pp. 31333–31349. DOI: https://doi.org/10.1029/1999JD900923. URL: https://agupubs.onlinelibrary.wiley.com/doi/abs/10.1029/1999JD900923.

García, R. D. et al. (2021). "Water Vapor Retrievals from Spectral Direct Irradiance Measured with an EKO MS-711 Spectroradiometer—Intercomparison with Other Techniques". In: *Remote Sensing* 13.5. ISSN: 2072-4292. URL: https://www.mdpi.com/2072-4292/13/3/350.

García-Cabrera, R. D. et al. (2019). "Characterization of an EKO MS-711 spectroradiometer: aerosol retrieval from spectral direct irradiance measurements and corrections of the circumsolar radiation". In: *Atmospheric Measurement Techniques.* DOI: https://doi.org/10.5194/amt-2019-467.

García-Cabrera, R. D. et al. (2020). “Aerosol retrievals from the EKO MS-711 spectral direct irradiance measurements and corrections of the circumsolar radiation”. In: *Atmospheric Measurement Techniques* 13.5. https://doi.org/10.5194/amt-13-2601-2020, pp. 2601–2621.

Hansen, J. et al. (2000). “Global warming in the twenty-first century: An alternative scenario”. In: *Proceedings of the National Academy of Sciences* 97.18, pp. 9875–9880. DOI: 10.1073/pnas.170278997. URL: https://www.pnas.org/doi/abs/10.1073/pnas.170278997.

IPCC (2022). *Climate Change 2022: Impacts, Adaptation and Vulnerability.* Summary for Policymakers. Cambridge, UK and New York, USA: Cambridge University Press, pp. 3–33. ISBN: 9781009325844.

Liu, C. et al. (2018). “The absorption Ängstrom exponent of black carbon: from numerical aspects”. In: *Atmospheric Chemistry and Physics* 18.9, pp. 6259–6273. DOI: 10.5194/acp-18-6259-2018. URL: https://acp.copernicus.org/articles/18/6259/2018/.

Long, C. N. and T. P. Ackerman (2000). “Identification of clear skies from broadband pyranometer measurements and calculation of downwelling shortwave cloud effects”. In: *Journal of Geophysical Research: Atmospheres* 105.D12, pp. 15609–15626. DOI: https://doi.org/10.1029/2000JD900077. URL: https://agupubs.onlinelibrary.wiley.com/doi/abs/10.1029/2000JD900077.

Michalsky, J. J. and P. W. Kiedron (2022). “Moderate spectral resolution solar irradiance measurements, aerosol optical depth, and solar transmission, from 360 to 1070 nm, using the refurbished rotating shadow band spectroradiometer (RSS)”. In: *Atmospheric Measurement Techniques* 15.2, pp. 353–364. DOI: 10.5194/amt-15-353-2022. URL: https://amt.copernicus.org/articles/15/353/2022/.

Michalsky, J. J., J. C. Liljegren, and L. C. Harrison (1995). “A comparison of sun photometer derivations of total column water vapor and ozone to standard measures of same at the Southern Great Plains atmospheric radiation measurement site”. In: *Journal of Geophysical Research* 100, pp. 25995–26003. DOI: https://doi.org/10.1029/95JD02706.

Michalsky, J. J., J. A. Schlemmer, et al. (2001). “Multiyear measurements of aerosol optical depth in the Atmospheric Radiation Measurement and Quantitative Links programs”. In: *Journal of Geophysical Research: Atmospheres* 106.D11, pp. 12099–12107. DOI: https://doi.org/10.1029/2001JD900096. URL: https://agupubs.onlinelibrary.wiley.com/doi/abs/10.1029/2001JD900096.

Michalsky, J.J., L.C. Harrison, and W.E. Berkheiser (1995). “Cosine response characteristics of some radiometric and photometric sensors”. In: *Solar Energy* 54.6, pp. 397–402. ISSN: 0038-092X. DOI: https://doi.org/10.1016/0038-092X(95)00017-L. URL: https://www.sciencedirect.com/science/article/pii/0038092X9500017L.

Mohr, K. and R. Holland (2023). *How Aerosols Are Measured: The Science of Deep Blue.* URL: https://earth.gsfc.nasa.gov/climate/data/deep-blue/science.

Myhre, G. et al. (2013). “Aerosols and their Relation to Global Climate and Climate Sensitivity”. In: *Nature Education Knowledge* 4. URL: https://www.nature.com/scitable/knowledge/library/aerosols-and-their-relation-to-global-climate-102215345/.

NOAA, Global Monitoring Laboratory (2022). *Solar Radiation Instrument Descriptions.* URL: https://gml.noaa.gov/grad/instruments.html.

NOAA, Global Monitoring Laboratory (2023). *SURFRAD Aerosol Optical Depth.* URL: https://gml.noaa.gov/grad/surfrad/aod/.

Ortenberg, F. (2002). *Ozone: Space Vision (Space monitoring of Earth Atmospheric Ozone).*

Pó, M. et al. (2018). "Direct Spectral Irradiance Measurements from Rotating Shadowband EKO Grating Spectroradiometer". In: *2018 IEEE 7th World Conference on Photovoltaic Energy Conversion (WCPEC) (A Joint Conference of 45th IEEE PVSC, 28th PVSEC 34th EU PVSEC)*, pp. 2337–2340. DOI: 10.1109/PVSC.2018.8547445.

Shaw, G. E. (1983). "Sun Photometry". In: *Bulletin of the American Meteorological Society* 64.1, pp. 4–10. DOI: https://doi.org/10.1175/1520-0477(1983)064<0004:SP>2.0.CO;2. URL: https://journals.ametsoc.org/view/journals/bams/64/1/1520-0477_1983_064_0004_sp_2_0_co_2.xml.

Smith III, F. L. and C. Smith (1972). "Numerical evaluation of Chapman's grazing incidence integral ch (X,)" in: *Journal of Geophysical Research* 77.19, pp. 3592–3597. DOI: https://doi.org/10.1029/JA077i019p03592. URL: https://agupubs.onlinelibrary.wiley.com/doi/abs/10.1029/JA077i019p03592.

Vignola, F, J Michalsky, and T. Stoffel (2019). *Solar and Infrared Radiation Measurements.* Second Editon. CRC Press, Taylor and Francis Group. ISBN: 978-1-138-09629-5. DOI: https://doi.org/10.1201/b22306.

Wild, M. (Mar. 2022). *Radiation and Climate Change. Radiation in Global Climate Model.* ETH Zürich.

WMO (2023). *Fifth WMO Filter Radiometer Comparison (FRC-V).* Tech. rep. 280. Global Atmosphere Watch (GAW).

1197 # Appendix

1198 # A Instrumentation

1199 ## A.1 SURFRAD network

1200 Figure A1 shows the location of the 7 SURFRAD stations across U.S. The EKO MS-711 instrument
1201 has been installed at Table Mountain, in Boulder, Colorado.

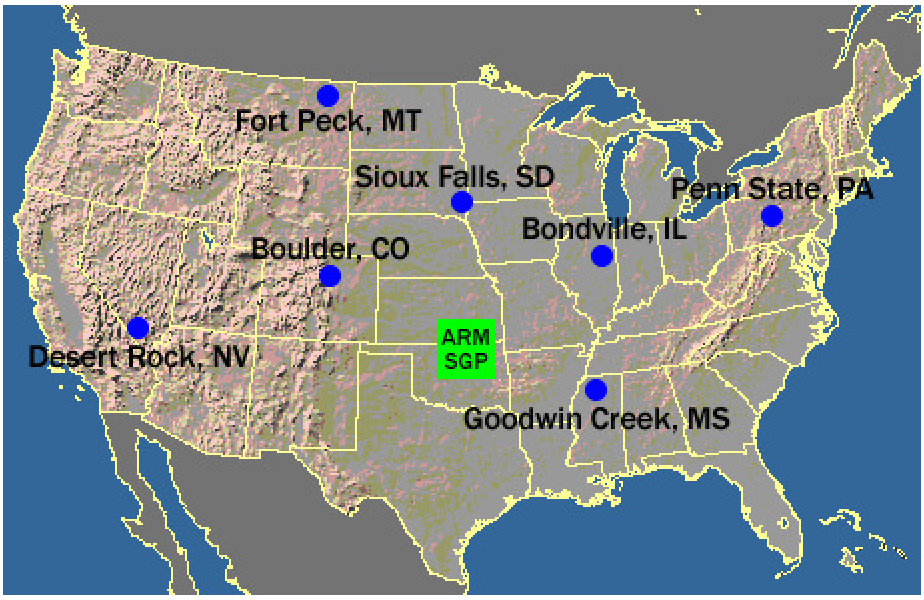

Figure A1: Map of the SURFRAD network across U.S.

A.2 Spectrometer configuration

Figure A2 shows the key components of a spectrometer.

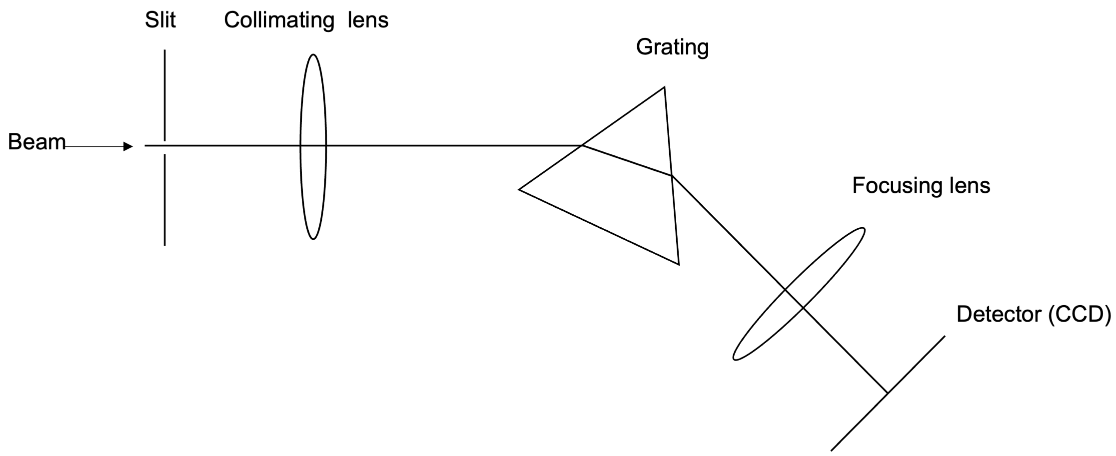

Figure A2: Schematic of the key components of a spectrometer. Adapted from Vignola, Michalsky, and Stoffel 2019.

First, the incoming beam hits the entrance slit. A collimating lens allows light coming out of the slit to become parallel (collimated) before reaching the grating, which splits the light into its individual wavelength components. A second lens focuses the light on the detector array, in this case a CCD, which is used to detect the intensity of photons at each corresponding wavelength (Vignola, Michalsky, and Stoffel 2019).

B Methods

B.1 Solar spectrum and absorption bands

Figure B1 shows the solar spectrum at the top of the atmosphere, at sea level, and a blackbody representing 5900°K.

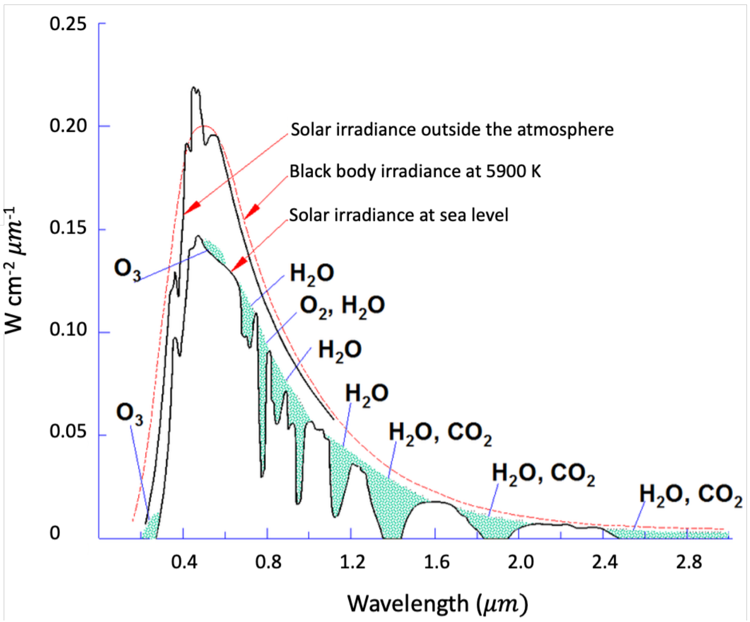

Figure B1: Solar spectrum at the top of the atmosphere, at sea level, and a blackbody representing 5900°K. Adapted from Ortenberg 2002.

In Figure B2a, the absorptivity of various atmospheric components is depicted across different wavelengths. Notably, ozone is the primary contributor in the MFRSR channels, particularly at 674 nm. Figure B2b shows the variation of the Rayleigh scattering as a function of the wavelength in the visible range. As the wavelength increases, the Rayleigh component decreases.

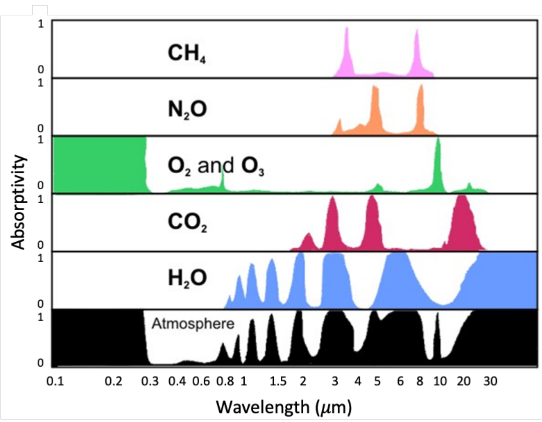

(a) Absorption spectra of various gases in the atmosphere. Adapted from Babb 2023.

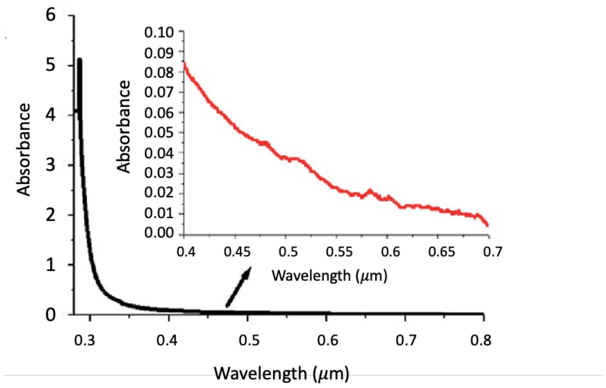

(b) Rayleigh scattering at different wavelength. Adapted from Benniston et al. 2014.

Figure B2: Absorption bands of different components in the atmosphere.

B.2 Cosine correction algorithm

Algorithm 1 outlines the procedure to apply the cosine correction to the computed DNI values (obtained from measured data) based on the manufacturer's specified Table 5.

Data: solar azimuth angle ϕ, DNI measured, south error equation (ϵ_{south}), north error equation (ϵ_{north}), east error equation ((ϵ_{east})), west error equation ((ϵ_{west}))

Result: DNI corrected

if $\phi > 0$ ***and*** $\phi \leq 90$ **then**

$\text{w}_{\text{east}} = \frac{\alpha}{90}$;

$\text{w}_{\text{north}} = \frac{90-\alpha}{90}$;

DNI corrected = DNI computed / (1 + ($\text{w}_{\text{east}} \cdot \epsilon_{\text{east}}$) + ($\text{w}_{\text{north}} \cdot \epsilon_{\text{north}}$));

else if $\phi > 90$ ***and*** $\phi \leq 180$ **then**

$\text{w}_{\text{east}} = \frac{180-\alpha}{90}$;

$\text{w}_{\text{south}} = \frac{\alpha-90}{90}$;

DNI corrected = DNI computed / (1 + ($\text{w}_{\text{east}} \cdot \epsilon_{\text{east}}$) + ($\text{w}_{\text{south}} \cdot \epsilon_{\text{south}}$));

else if $\phi > 180$ ***and*** $\phi \leq 270$ **then**

$\text{w}_{\text{west}} = \frac{\alpha-180}{90}$;

$\text{w}_{\text{south}} = \frac{270-\alpha}{90}$;

DNI corrected = DNI computed / (1 + ($\text{w}_{\text{west}} \cdot \epsilon_{\text{west}}$) + ($\text{w}_{\text{south}} \cdot \epsilon_{\text{south}}$));

else if $\phi > 270$ ***and*** $\phi \leq 360$ **then**

$\text{w}_{\text{west}} = \frac{360-\alpha}{90}$;

$\text{w}_{\text{north}} = \frac{\alpha-270}{90}$;

DNI corrected = DNI computed / (1 + ($\text{w}_{\text{west}} \cdot \epsilon_{\text{west}}$) + ($\text{w}_{\text{north}} \cdot \epsilon_{\text{north}}$));

Algorithm 1: Solar Azimuth Correction Algorithm.

C Results

Figure C1 shows the comparison between AOD derived from raw data and AOD from slit-corrected data. Shown are the results for 415 nm, 674 nm and 868 nm for September 27th, 2023.

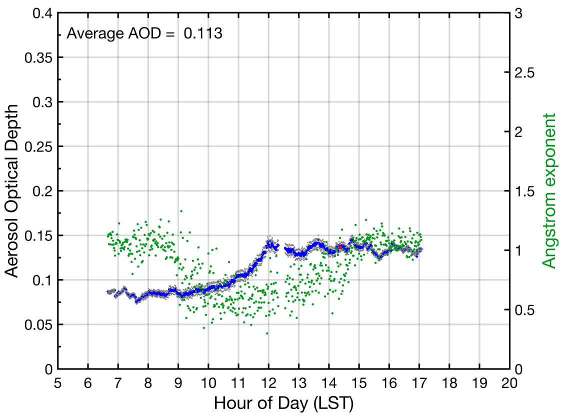

(a) 415 nm

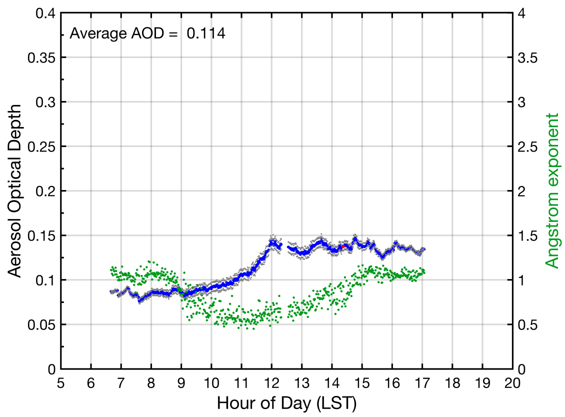

(b) 415 nm

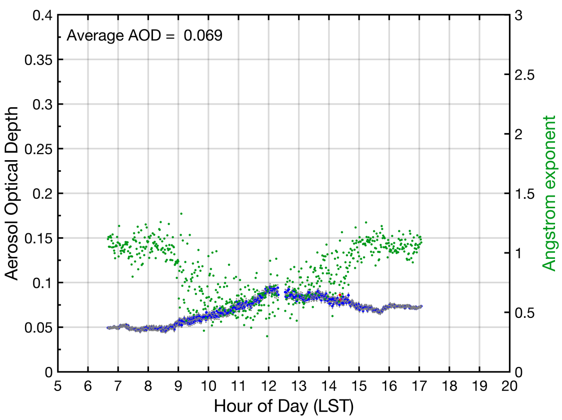

(c) 674 nm

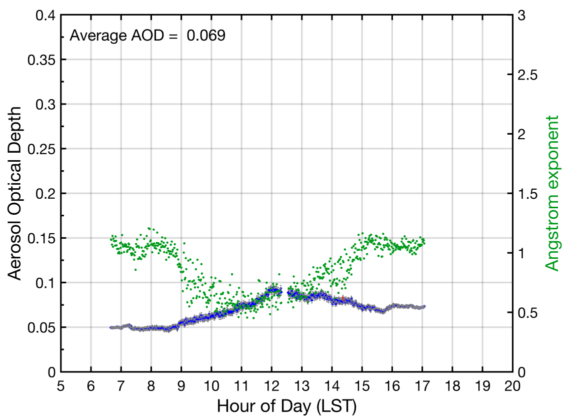

(d) 674 nm

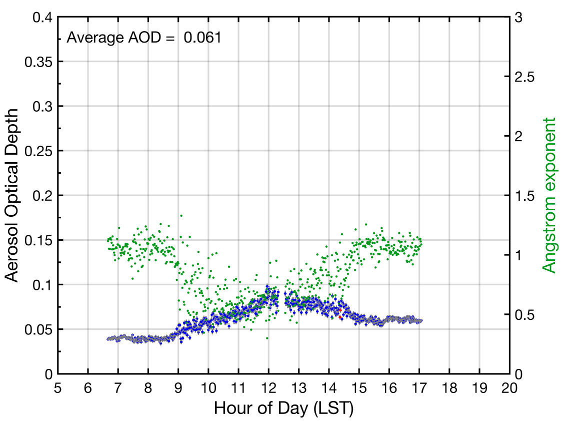

(e) 868 nm

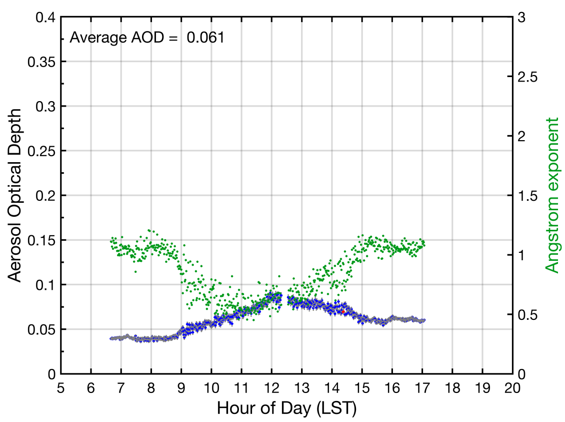

(f) 868 nm

Figure C1: AOD (in blue) retrieved from raw data (right) and from slit-corrected data (left) for September 27th, 2023. Green points represent the Ängstrom exponent, gray dots the AOD error.

Figure C2 depicts the correlation between AOD from MFRSR (y-axis) and EKO MS-711 (x-axis) for the 4 channels. In these plots the manufacturer's cosine correction has been applied to DNI slit-corrected data collected by EKO MS-711.

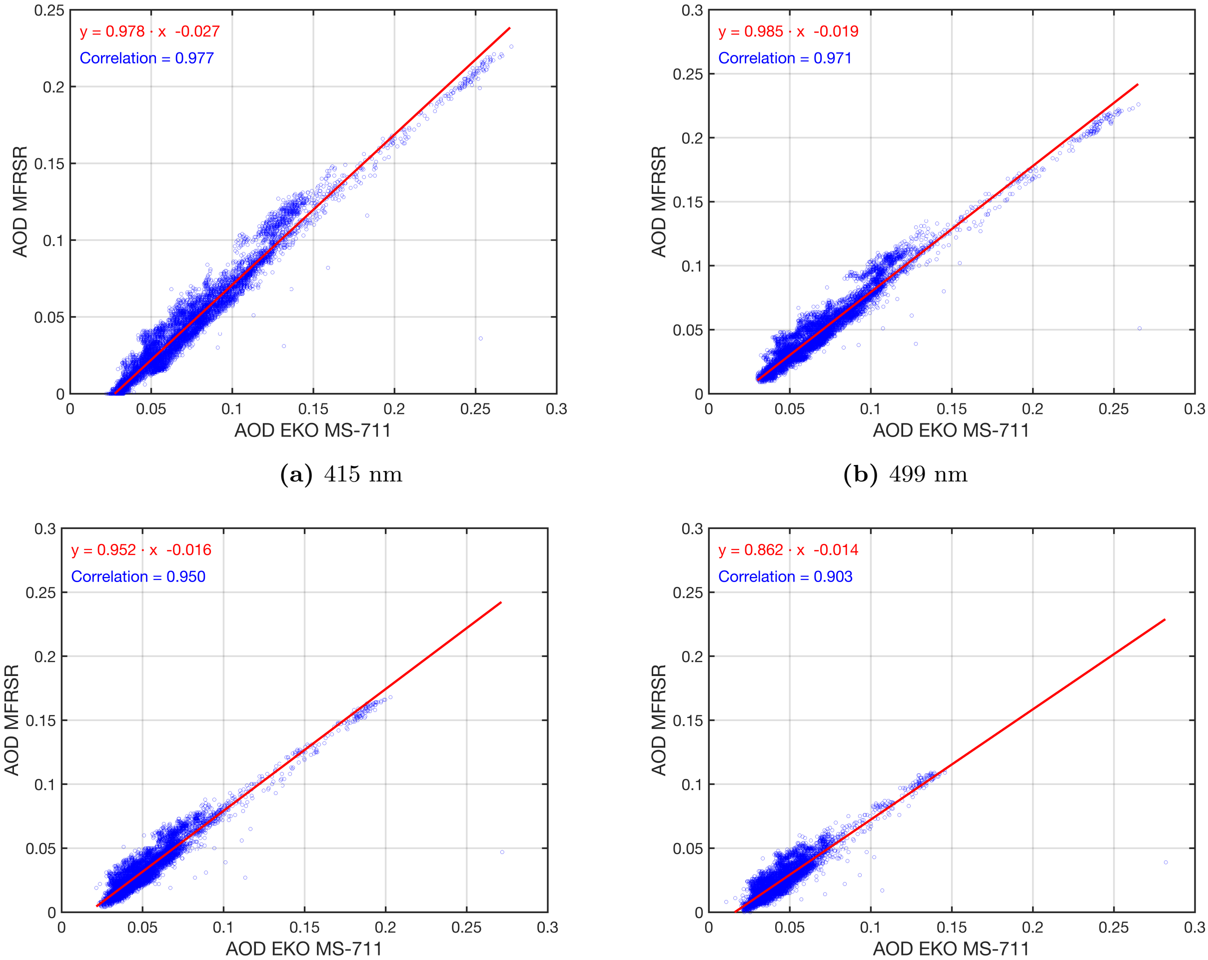

(a) 415 nm **(b)** 499 nm

(c) 674 nm **(d)** 868 nm

Figure C2: Correlation between AOD values retrievd from the MFRSR (y-axis) and from the EKO MS-711 (x-axis). Results for the 4 channels are presented. The manufacturer's cosine correction has been applied to DNI slit-corrected data collected by EKO MS-711.

The correlation between AOD from MFRSR (y-axis) and EKO MS-711 (x-axis) for the 4 channels is illustrated by the Figure C3. No cosine correction has been applied to DNI slit-corrected data collected by EKO MS-711.

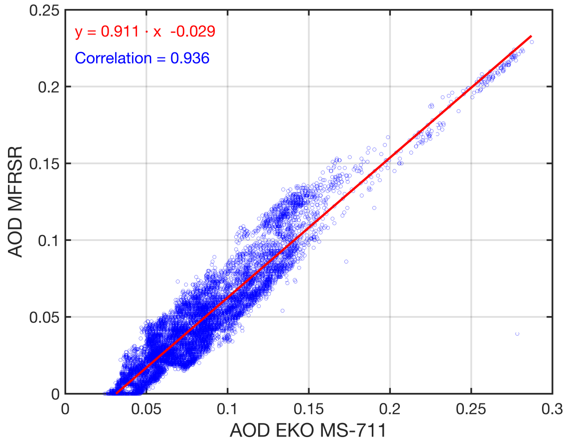

(a) 415 nm

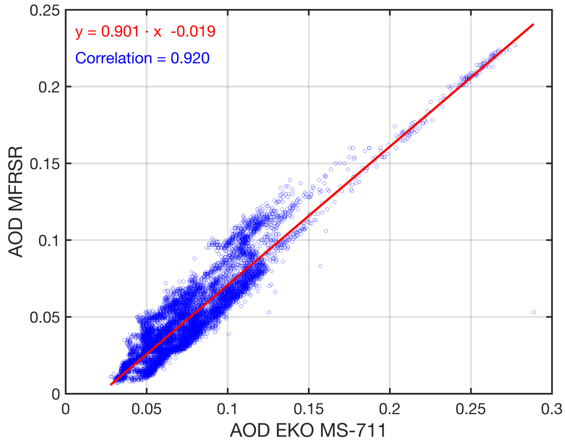

(b) 499 nm

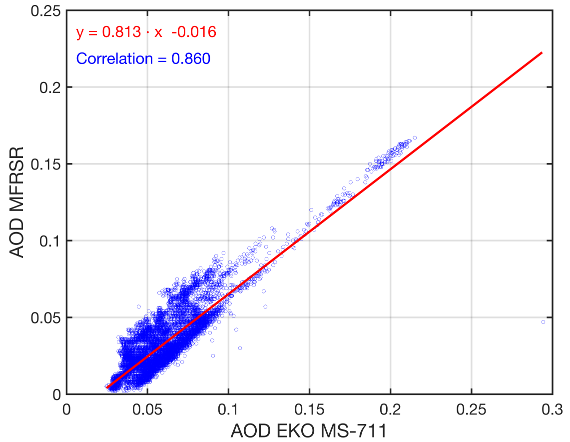

(c) 674 nm

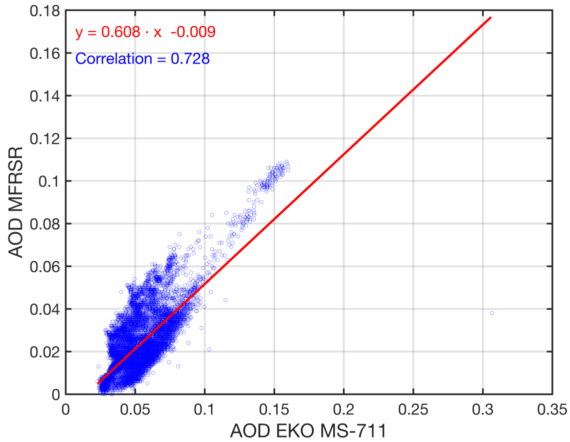

(d) 868 nm

Figure C3: Correlation between AOD values retrievd from the MFRSR (y-axis) and from the EKO MS-711 (x-axis). Results for the 4 channels are presented. No cosine correction has been applied to DNI slit-corrected data collected by EKO MS-711.

1231 Figure C4 represents the the percentage difference between the ratio diffuse to global irradiance
1232 measured by MFRSR and EKO MS-711 with respect to the EKO MS-711 ratio.

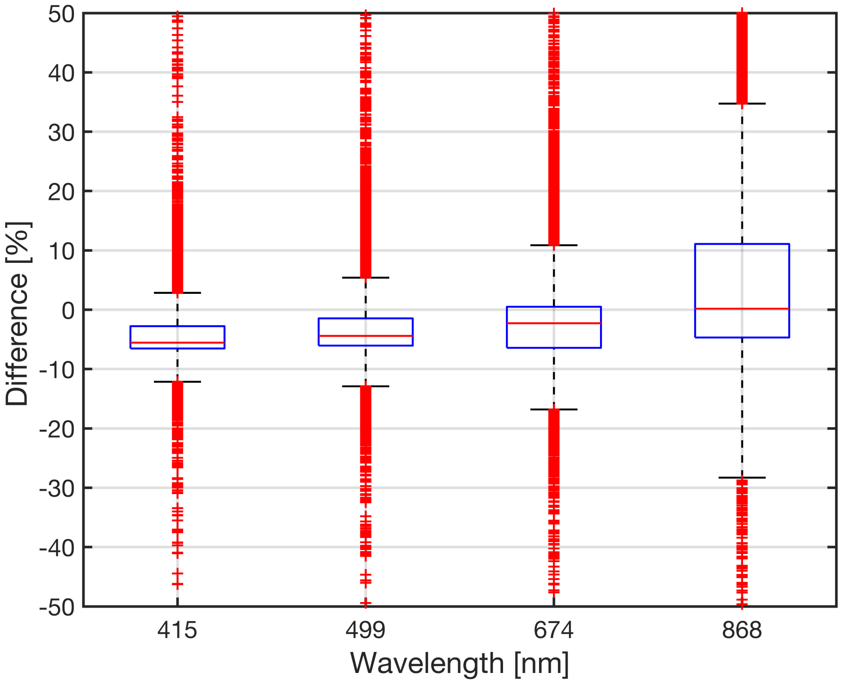

Figure C4: Difference in the ratio DHI/GHI (%) between MFRSR and EKO MS-711 with respect to EKO MS-711.

Table C1 reports for the 4 channels the extrapolated $\ln(V_0)$ as well as the total optical depth for the Langley days based on data obtained from the EKO MS-711. A distinction between morning and afternoon is made.

Table C1: V_0 extrapolation (y-intercept) and total optical depth (slope) for selected *clear-sky* days, September-October 2023.

Date	**Extrapolated $\ln(V_0)$**				$\sum \tau$			
	415 nm	499 nm	674 nm	868 nm	415 nm	499 nm	674 nm	868 nm
Morning								
20 Sept.	7.440	7.600	7.333	6.859	0.307	0.171	0.075	0.034
24 Sept.	7.418	7.584	7.324	6.854	0.297	0.163	0.071	0.031
25 Sept.	7.424	7.591	7.330	6.855	0.307	0.171	0.075	0.034
26 Sept.	7.393	7.567	7.322	6.857	0.342	0.196	0.090	0.045
27 Sept.	7.438	7.604	7.339	6.862	0.332	0.187	0.082	0.037
28 Sept.	7.402	7.578	7.324	6.853	0.303	0.167	0.070	0.030
7 Oct.	7.445	7.609	7.344	6.871	0.287	0.154	0.064	0.025
8 Oct.	7.459	7.624	7.357	8.877	0.290	0.158	0.069	0.028
9 Oct.	7.443	7.607	7.341	6.868	0.301	0.163	0.068	0.028
10 Oct.	7.407	7.581	7.328	6.853	0.276	0.146	0.059	0.020
13 Oct.	7.429	7.603	7.343	6.873	0.293	0.162	0.072	0.030
15 Oct.	7.439	7.604	7.340	6.868	0.289	0.154	0.063	0.024
16 Oct.	7.452	7.614	7.346	6.868	0.283	0.150	0.060	0.022
17 Oct.	7.429	7.600	7.344	6.867	0.270	0.143	0.059	0.022
18 Oct.	7.387	7.573	7.320	6.850	0.273	0.147	0.060	0.023
19 Oct.	7.428	7.596	7.334	6.858	0.267	0.139	0.053	0.018
20 Oct.	7.444	7.613	7.352	6.876	0.263	0.137	0.053	0.018
21 Oct.	7.441	7.613	7.351	6.877	0.272	0.144	0.058	0.022
22 Oct.	7.425	7.599	7.348	6.880	0.316	0.178	0.082	0.041
25 Oct.	7.442	7.607	7.346	6.875	0.312	0.172	0.075	0.034
Afternoon								
22 Sept.	7.435	7.595	7.325	6.845	0.327	0.188	0.086	0.043
24 Sept.	7.425	7.586	7.323	6.845	0.316	0.176	0.076	0.033
25 Sept.	7.419	7.581	7.321	6.388	0.317	0.177	0.077	0.035
26 Sept.	7.489	7.634	7.355	6.864	0.402	0.240	0.115	0.062
27 Sept.	7.428	7.596	7.337	6.858	0.377	0.220	0.102	0.055
5 Oct.	7.383	7.554	7.303	6.835	0.306	0.164	0.065	0.025
7 Oct.	7.443	7.602	7.333	6.856	0.300	0.162	0.065	0.025
8 Oct.	7.440	7.598	7.329	6.851	0.297	0.158	0.062	0.023
13 Oct.	7.396	7.566	7.307	6.838	0.289	0.152	0.057	0.018
15 Oct.	7.450	7.609	7.335	6.856	0.306	0.163	0.062	0.021
16 Oct.	7.450	7.610	7.343	6.864	0.301	0.162	0.066	0.029
19 Oct.	7.438	7.605	7.342	6.866	0.282	0.150	0.060	0.026
20 Oct.	7.441	7.603	7.342	6.864	0.293	0.158	0.067	0.032
25 Oct.	7.490	7.640	7.365	6.881	0.372	0.217	0.099	0.046

As above, Table C2 lists $\ln(V_0)$ and $\sum\tau$ for the 4 channels. MFRSR data are considered.

Table C2: V_0 extrapolation (y-intercept) and total optical depth (slope) for selected *clear-sky* days, September-October 2023. MFRSR value

Date	**Extrapolated ln(V_0)**				$\sum\tau$			
	415 nm	499 nm	674 nm	868 nm	415 nm	499 nm	674 nm	868 nm
Morning								
20 Sept.	7.484	7.297	6.983	7.237	0.289	0.163	0.067	0.025
24 Sept.	7.467	7.291	6.985	7.240	0.282	0.161	0.068	0.026
25 Sept.	7.476	7.297	6.991	7.244	0.293	0.168	0.072	0.029
26 Sept.	7.431	7.265	6.975	7.237	0.324	0.192	0.085	0.038
27 Sept.	7.489	7.306	6.998	7.249	0.320	0.186	0.080	0.034
28 Sept.	7.449	7.277	6.978	7.234	0.291	0.164	0.067	0.025
7 Oct.	7.473	7.291	6.984	7.241	0.272	0.149	0.058	0.020
8 Oct.	7.496	7.316	7.005	7.255	0.277	0.156	0.064	0.024
9 Oct.	7.476	7.300	6.993	7.246	0.286	0.161	0.064	0.024
10 Oct.	7.450	7.282	6.984	7.240	0.264	0.146	0.058	0.020
13 Oct.	7.457	7.289	6.987	7.246	0.277	0.158	0.066	0.027
15 Oct.	7.466	7.288	6.986	7.241	0.274	0.150	0.059	0.021
16 Oct.	7.495	7.313	7.001	7.252	0.273	0.150	0.058	0.021
17 Oct.	7.476	7.297	6.992	7.249	0.260	0.141	0.055	0.019
18 Oct.	7.427	7.265	6.970	7.228	0.261	0.144	0.057	0.020
19 Oct.	7.471	7.290	6.985	7.239	0.256	0.135	0.049	0.014
20 Oct.	7.471	7.290	6.985	7.241	0.248	0.130	0.046	0.012
21 Oct.	7.470	7.289	6.987	7.242	0.257	0.137	0.051	0.015
22 Oct.	7.452	7.283	6.991	7.250	0.300	0.174	0.078	0.036
23 Oct.	7.476	7.300	6.998	7.252	0.297	0.170	0.073	0.031
Afternoon								
22 Sept.	7.488	7.304	6.994	7.250	0.326	0.198	0.100	0.056
24 Sept.	7.488	7.304	6.995	7.252	0.319	0.191	0.091	0.049
25 Sept.	7.475	7.295	6.989	7.246	0.319	0.191	0.092	0.050
26 Sept.	7.536	7.344	7.025	7.271	0.399	0.252	0.130	0.076
27 Sept.	7.489	7.315	7.013	7.267	0.378	0.235	0.119	0.069
5 Oct.	7.449	7.279	6.987	7.250	0.314	0.184	0.087	0.046
7 Oct.	7.497	7.313	7.005	7.259	0.304	0.177	0.081	0.040
8 Oct.	7.496	7.309	6.998	7.252	0.300	0.172	0.076	0.037
13 Oct.	7.445	7.270	6.979	7.241	0.297	0.171	0.079	0.040
15 Oct.	7.513	7.325	7.011	7.260	0.313	0.181	0.081	0.039
16 Oct.	7.516	7.328	7.024	7.274	0.308	0.179	0.085	0.046
19 Oct.	7.502	7.316	7.015	7.269	0.289	0.164	0.077	0.042
20 Oct.	7.491	7.310	7.008	7.263	0.294	0.170	0.081	0.045
25 Oct.	7.571	7.378	7.056	7.300	0.386	0.245	0.126	0.072

Figure C5 shows MFRSR calibration Langley slope ($\sum\tau$ values) against the EKO MS-711 calibration slope. For every channel, morning and afternoon values are represented separately, in blue and magenta respectively.

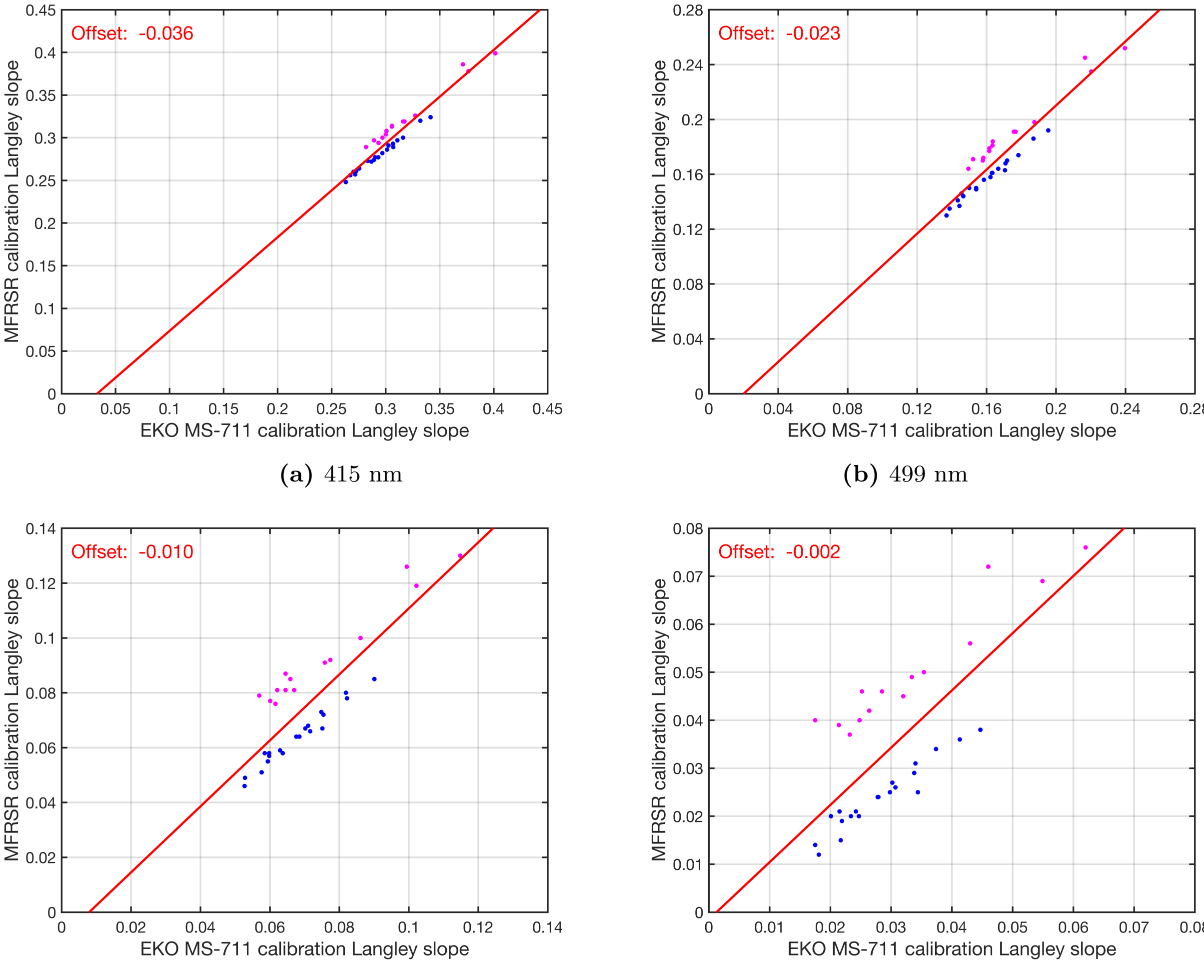

(a) 415 nm

(b) 499 nm

(c) 674 nm

(d) 868 nm

Figure C5: Comparison of the Langley slopes $\sum\tau$ obtained with the Langleys, MFRSR (y-axis) versus EKO MS-711 (x-axis). Blue points represent morning values, magenta points afternoon slopes.

Figures C6, C7, C8 and C9 show the V_0 calibration time series and linear fit for MFRSR (left) and EKO MS-711 (right) for the Langley calibration days. The V_0 equation is displayed, as well as the total τ error.

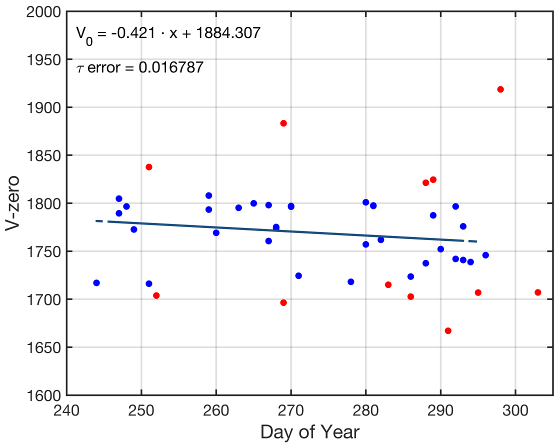

(a) MFRSR

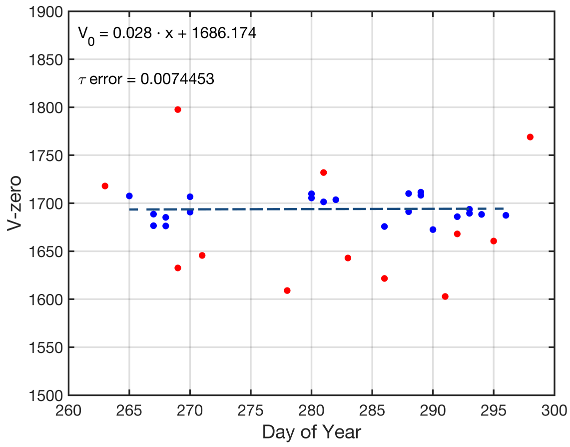

(b) EKO MS-711

Figure C6: V_0 calibration time series and linear fit for MFRSR (left) and EKO MS-711 (right), 415 nm.

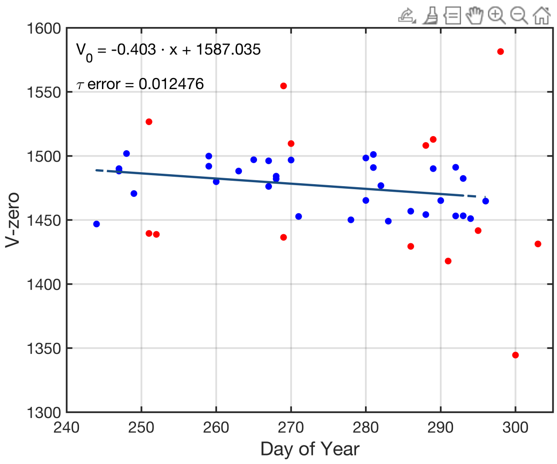

(a) MFRSR

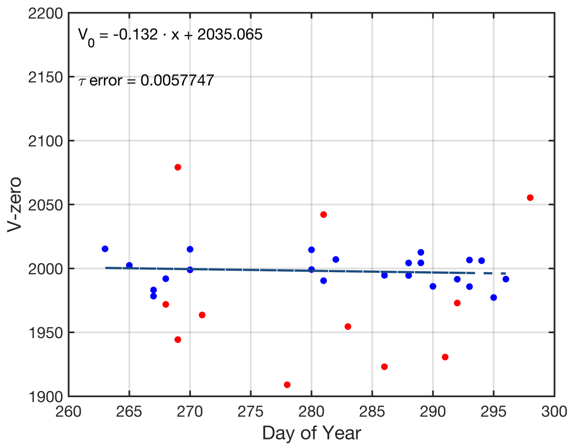

(b) EKO MS-711

Figure C7: V_0 calibration time series and linear fit for MFRSR (left) and EKO MS-711 (right), 499 nm.

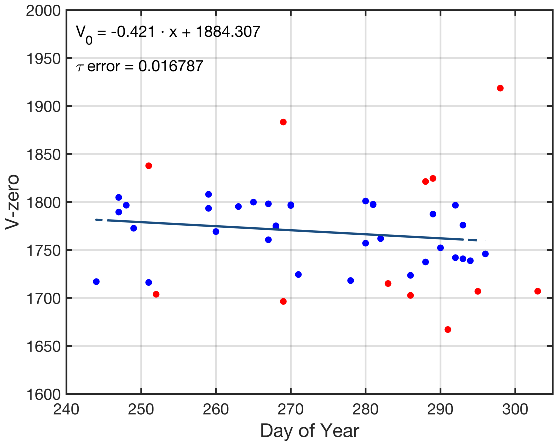

(a) MFRSR

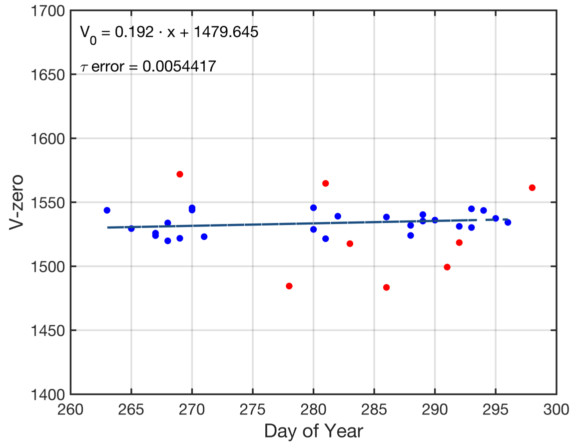

(b) EKO MS-711

Figure C8: V_0 calibration time series and linear fit for MFRSR (left) and EKO MS-711 (right), 674 nm.

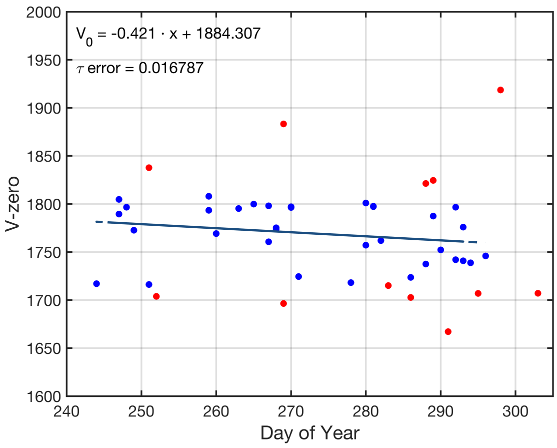

(a) MFRSR

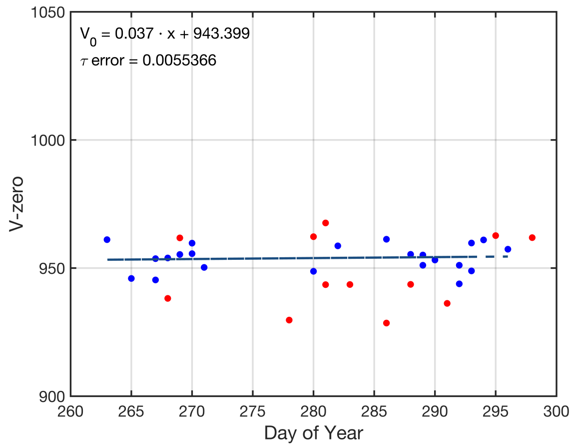

(b) EKO MS-711

Figure C9: V_0 calibration time series and linear fit for MFRSR (left) and EKO MS-711 (right), 868 nm.

Figure C10 shows the frequency distribution of the V_0 values for the EKO MS-711.

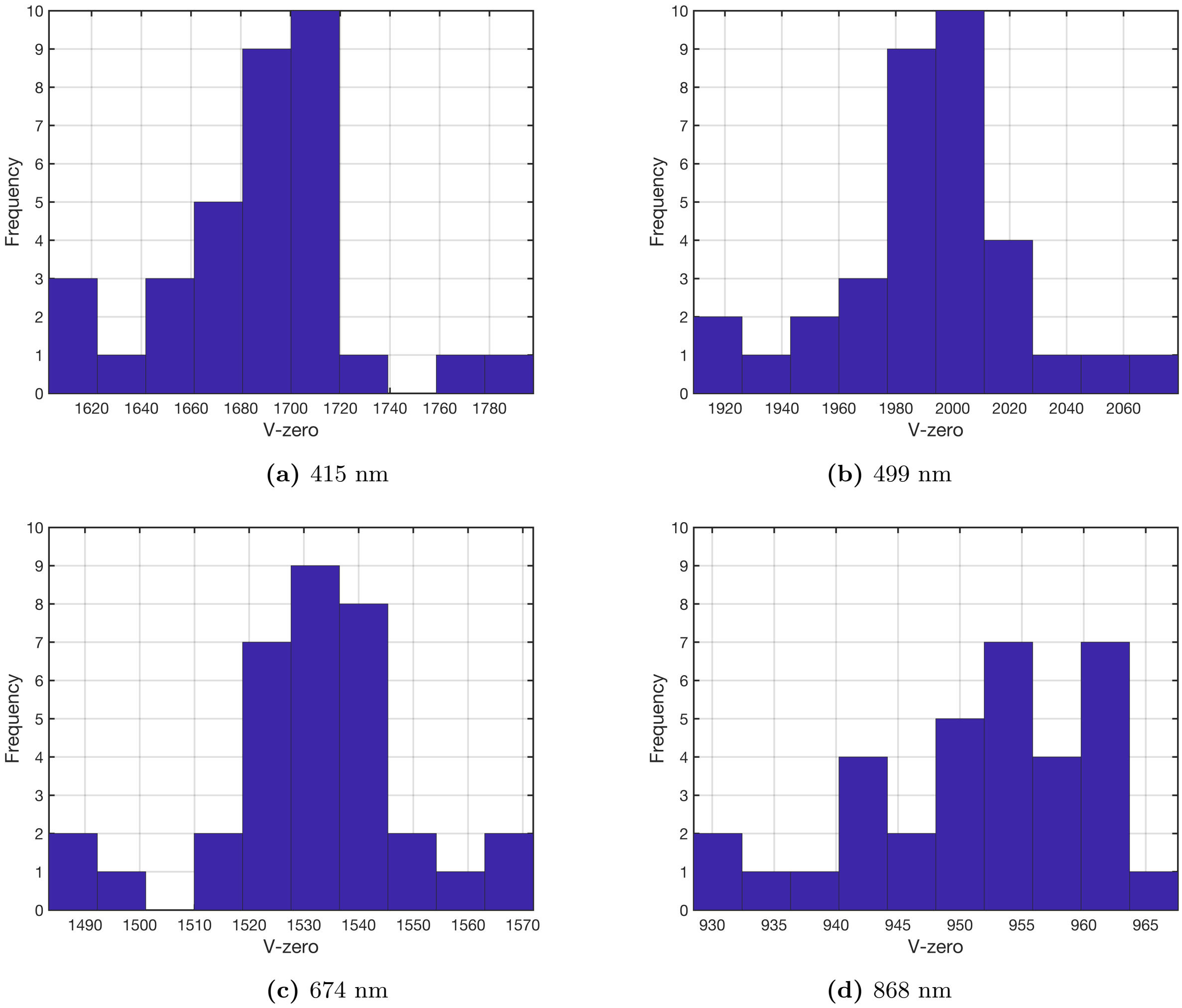

(a) 415 nm

(b) 499 nm

(c) 674 nm

(d) 868 nm

Figure C10: Frequency distribution of the $V_{0 \text{ values}}$ for the EKO MS-711.

Figure C11 shows the logarithm of AOD versus the logarithm of wavelength for the MFRSR at noon. From left to right, the red dots represent 415 nm, 499 nm, 674 nm and 868 nm respectively. A consistent pattern can be seen, namely the fact that the 415 nm channel is misaligned with the other channels. This does not affect the computation of the Ängstrom exponent itself, but it highlights that AOD retrieval for that channel may be problematic.

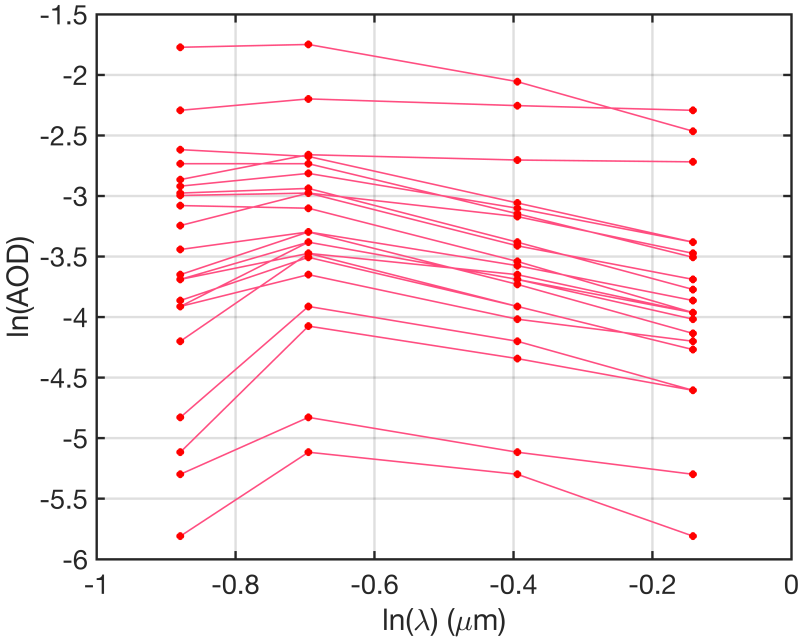

Figure C11: Logarithm of AOD versus logarithm of wavelength for the MFRSR. From left to right, the red dots represent 415 nm, 499 nm, 674 nm and 868 nm respectively. The slope of a line between the second (499 nm) and fourth (868 nm) points of each plotted line represents the Ängstrom exponent α.